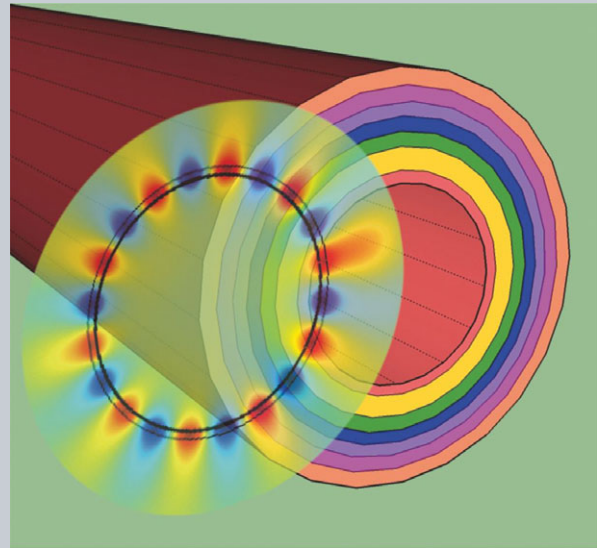


Abstract Optical microcavities with whispering-gallery modes (WGMs) have large potential and, in particular, those with a tubular geometry have attracted increasing attention due to their special geometry and interesting properties such as trimmed resonant modes, simplicity as fluidic channels, three-dimensionally (3D) mode confinement, unique evanescent wave, and so on. Optical microcavities with the tubular geometry meet the challenge of assembly of conductive, semiconductive and insulating materials into a tubular geometry, thus spurring multifunctional applications to optofluidic devices, optical microdevices like microlasers, and bio/chemical sensors. Fabrication methods such as the fiber-drawing method, rolled-up nanotechnology, electrospin technique, and template-assisted method have been developed to address the various requirements. These tubular optical microcavities enable researchers to explore and construct novel optical microdevices for a wide range of potential applications. This review describes the tubular optical microcavities from the perspectives of theoretical consideration, optical characterization, and potential applications.



Optical microcavities with tubular geometry: properties and applications

Jiao Wang^{1,2}, Tianrong Zhan¹, Gaoshan Huang¹, Paul K. Chu², and Yongfeng Mei^{1,*}

1. Introduction to tubular microcavities

Miniaturization and integration are hot research topics in modern optics and related fields [1–4] and optical resonators are ubiquitous in modern optics and optical devices [1]. A variety of cavity resonator geometries, including Fabry–Pérot resonators, photonic crystal resonators and whispering-gallery mode (WGM) resonances, has been fabricated [5, 6]. These resonators constitute attractive physical systems suitable for basic studies and applications [5, 6] and consequently, the associated fabrication methods and materials properties are extensively investigated. Optical microcavities can be produced by lithographic methods [7], the fiber-drawing technique [8], and self-rolled-up processes [9]. Despite the versatility, traditional Fabry–Pérot resonators and photonic crystal resonators, including the folded or ring varieties, are fairly complex, large, difficult to assemble, and prone to vibration instability because of low-frequency mechanical resonances [3]. In many applications, the stability and small modal volume are of great importance, but miniaturization of conventional Fabry–Pérot resonators is very complicated or yields low quality factors (Q-factor) [3]. Microcavities based on photonic crystals can provide extremely small mode volumes, but the Q-factors are typically well below the theoretical optimum. Hence, WGMs resonators with high Q-factor and high sensitivity

are attracting great research interest, due to the tunable size as well as easy assembly and fabrication.

WGMs resonators are typically dielectric spherical structures in which waves are confined by continuous total internal reflections. Compared to other types of optical resonators, WGMs resonators exhibit superior properties such as ultrahigh Q-factor and tunable size. Daniel Colladon and Jacques Babinet first demonstrated the idea in the 1840s that a light wave might be guided by continuous total internal reflection in water or glass and this discovery spurred the fabrication of new optics [10]. The WGM phenomenon was first described in the acoustic regime of St Paul's Cathedral in London by Lord Rayleigh [11] and research on WGMs was later extended to the radiofrequency and optical domains. A light wave can undergo reflection, refraction, and diffraction just as an acoustical wave travels along the surface of a wall. If the light path is curved below a certain minimum radius, as in a whispering gallery, the normal optical mode becomes WGM and the waveguide is named as a whispering-gallery guide. A light ray in a normal waveguide, such as an optical fiber, requires reflection from the inner surface to propagate. On the other hand, a light ray in a whispering-gallery waveguide requires reflection from the curved outer surface only, and so WGMs, sometimes are also referred to as morphology-dependent resonances (MDRs).

¹ Department of Materials Science, Fudan University, Shanghai, 200433, P. R. China

² Department of Physics and Materials Science, City University of Hong Kong, Tat Chee Avenue, Kowloon, Hong Kong, China

*Corresponding author(s): e-mail: yongfeng.mei@gmail.com

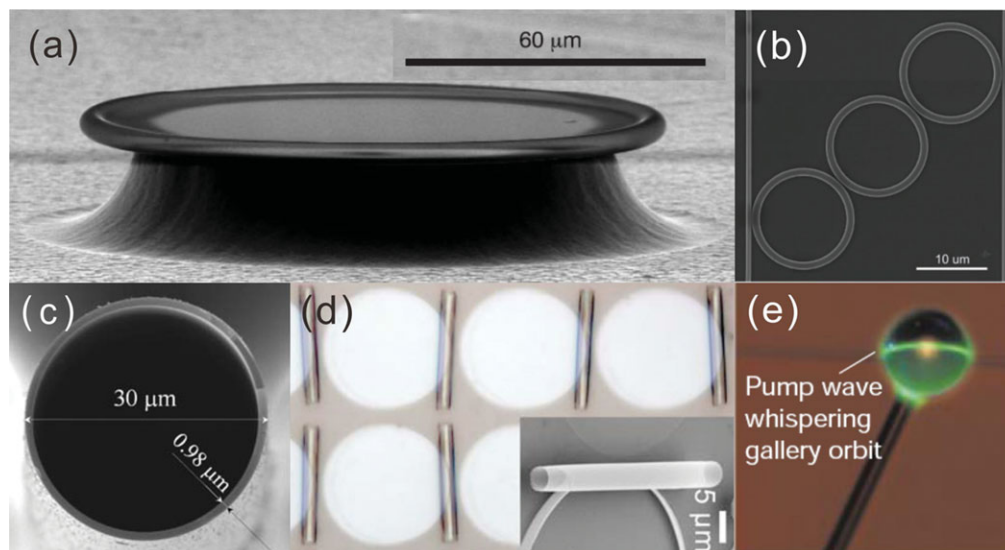


Figure 1 Various WGMs resonator configurations: (a) microtoroid [19], (b) slot waveguide ring resonator [20,21], (c) capillary-based microtubular resonator fabricated by the drawing method [22], (d) microtubular resonator fabricated by self-rolled-up processes [34], and (e) microsphere [6].

WGMs with morphology-dependent properties can aid the measurement of size, shape, refractive index, and temperature of a sphere as well as the diameter and mechanical deformation of fibers [2, 3, 12]. The strong influence of WGMs on fluorescence and Raman scattering has been recognized and used to fabricate microdevices such as biochemical sensors [13], microlasers [14, 15], temperature sensors [16], and so on [12]. Quasicontinuous-pumped lasing based on WGMs spherical cavity lasing was reported and the underlying theories were derived in 1961 [17]. The lasing behavior in a free dye-doped droplet was first reported in 1984 [18]. The WGMs phenomenon was later investigated in microdisk diode lasers and cylindrical polymer lasers and recently, WGMs resonance has been studied in various different systems. Figure 1 shows some of the popular types of WGMs resonance including the microtoroid [19], microring [20,21], tubular geometries [22], and spheres [6, 23, 24] and a variety of materials encompassing polymers [25–28], liquids [18, 29], inorganic species [30], and diamond [31, 32] can be used to fabricate WGM resonances. In this review, we will focus on optical microcavities with a tubular geometry and details of other types of WGMs optical microresonators can be found in other review papers [2, 3, 5, 6, 12, 20, 21, 33].

The advent of tubular optical microcavities has led to new generations of integrated devices and sensors [9, 35–38]. The first observation of a thin-film ring (tubular geometry) laser from a layered microcavity layer was reported by using a tubular glass rod covered with a rhodamine 6G (Rh 6G)-doped, 0.8- μm thick, light-guiding polyurethane film in 1971 [39]. Since then, various dye-doped/undoped transparent materials were chosen to prepare tubular microcavity structures by depositing thin films such as polyurethane, epoxy, lead-silica, gelatin, and polymethylmethacrylate (PMMA) on glass fibers [40]. Interfer-

ence modulation was observed from a layered microtube by Knight et al. [41,42]. These microcavities provide superior two-dimensional optical confinement with Q values in excess of 10^6 and bode well for low laser thresholds. The fused-silica capillary tube is filled with a dye-doped liquid having a high refractive index and this type of microcavity laser is called a core-resonance capillary-fiber WGMs laser [41,42]. The hollow microstructure (microsphere) was suggested by Artemyev et al. as a start to study three-dimensionally (3D) confined photonic and electronic states especially in the visible spectral range [43]. The layered microtubes additional boundaries introduce interference or guiding effects to modify the cavity modes significantly. On the heels of the rapid development of nanotechnology and nanoscience, highly luminescent quantum dots have been introduced to microcapillary microlaser systems [44]. Micro/nanotubes were first prepared via self-rolled-up nanotechnology [45, 46], followed by the study of Kipp et al. in 2006 on tubular WGM optical microcavities fabricated by self-rolling [47]. 3D optical confinement was observed along the microtube axis direction of self-rolled microtubular resonators in 2008 [48]. Afterwards, optofluidic devices based on a combination of microfluidic and optics have emerged and found applications in biological/chemical sensors [49], microlasers [50, 51], and temperature sensors [16]. The bottle microcavities with axis optical confinement were fabricated by Sumetsky, Rauschenbeutel and coworkers [14, 52, 53]. On account of the superior optical properties in these microtubular cavities, cell scaffolds, liquid refractive-index sensors, and low-threshold microlasers have been produced following the study of the optical resonance in self-rolled microtubular cavities. With the exception of the self-rolling method, most traditional techniques involve templates [54] and electrospinning [55] in the fabrication of microdevices or microsystems with good optical

performance [15] and promising applications [56] in DNA detection [50, 57], bio/chemsensing [49], cell cultures [36], lasing [29, 58], and integrated lab-on-a-chip/lab-in-a-tube devices [38]. Development of new fabrication processes and introduction of new materials have brought new functions [56]. The WGMs optical microcavities with a tubular geometry constitute the main topic of this review. The fabrication, optical properties, simulation methods, and potential applications of tubular optical microresonators are described in detail, followed by a description of future developments in this burgeoning field.

2. Theoretical consideration of tubular microresonators

Theoretical derivation is quite important to the design, fabrication, and applications of WGM microcavities with a tubular geometry as a tool to verify experimental data and design of optical microdevices. These WGM microcavities possess different optical resonating structures and analytical treatment is typically conducted with some approximations. For instance, microtubes can be regarded as multilayered cylindrical structures and structural imperfections in the wall of the microtubes are frequently ignored. To describe the optical properties of microtubes in the general cases, numerical simulation is necessary. Analytical and numerical results can impart complementary information about the optical resonance modes such as the resonance wavelength, Q-factor, and mode profile, which aid the design of WGM resonators.

Various computational methods have been proposed and implemented by solving Maxwell's equations. With regard to microtubes, besides the widely used analytical methods including waveguide approximation and Mie scattering, numerical methods such as the finite-difference time-domain method (FDTD), finite-element method (FEM) and boundary-element method (BEM) are used for the theoretical simulation of tubular microcavities. Numerical methods fall into two main categories. The first is the differential equation scheme including the FDTD and FEM methods, which involve discretizing the entire space in terms of grids and solving Maxwell's equations at each point in the grids. These approaches are quite flexible and suitable for objects with arbitrary shape. The second one is the integral equation scheme such as the BEM method. It involves dividing the structure into separate homogeneous regions and only boundary values at interfaces between different regions instead of values throughout the space are calculated. The latter approach is more efficient in terms of computational resources and suitable for problems concerning small surface/volume ratios. Numerical techniques and analytical models are complementary. Although numerical simulation can be used to simulate the optical properties of microtubes, analytical models are needed to explore the underlying mechanisms. The Mie scattering and adiabatic approximation methods are good analytical models providing insight into the optical properties of tubular microcavities.

In this section, we review the numerical methods for microtubes and the advantages, disadvantages, and the outlook of each method are discussed.

2.1. Finite-difference time-domain method

The finite-difference time-domain method (FDTD) method is widely used in optical calculations [59, 60]. In this technique, Maxwell's equations are converted into finite-difference equations by discretizing the time and space in finite grids. The resulting finite-difference equations are solved in a leapfrog manner. The FDTD method can be applied to complicated structures composed of different materials with arbitrary structural features. However, the computational time and memory can be demanding when spatial grid discretization must be sufficiently fine to capture the geometric details in the simulated structure. For example, when considering round objects, fine spatial grids must be used to resolve the curvature of bent boundaries.

To simulate microtubes using the FDTD method, the computational domain, geometry of the structure, grid size (time step), and boundary conditions are taken into consideration. To ensure the convergence of results in general cases, the size of the spatial grid δ and time step Δt should satisfy the following relationship:

$$\delta < \lambda/8, \Delta t < T/12, \quad (1)$$

and $\Delta t < \delta/c\sqrt{2}$, where λ and T are the wavelength and period of electromagnetic waves, respectively, and c is the speed of light in air. To model the problem in the simulation domain with a finite size, the proper boundary conditions such as periodical and absorbing boundary conditions are needed. The absorbing boundary conditions based on the perfect matched layer (PML) [61, 62] are widely used to suppress spurious reflection at the boundary of the computation domain. Using the FDTD method, the characteristics of optical resonances in the microtubes such as the resonance wavelength and Q-factor can be obtained by analyzing the temporal response of the system excited by a short optical pulse. The mode profile at resonance can be calculated accordingly by exciting the resonance mode using a chromatic point source. Additionally, it is convenient to track the evolution or propagation of light inside the microtubes. For example, Hosoda and Shigaki investigated the effects of notches of the microtubes on the resonance modes [63] and Kipp and coworkers studied 3D optical confinement in the microtubes with an uneven axial profile [48].

Although previous works mainly focus on optical resonances in microtubes made of passive materials, the lasing action in microtubes incorporated with gain media have attracted considerable attention. Many experimental results have recently been obtained and in fact, it is possible to study this problem numerically by the FDTD method [64, 65].

To model the gain media, we consider an effective four-level atomic system with transition occupation numbers N_i

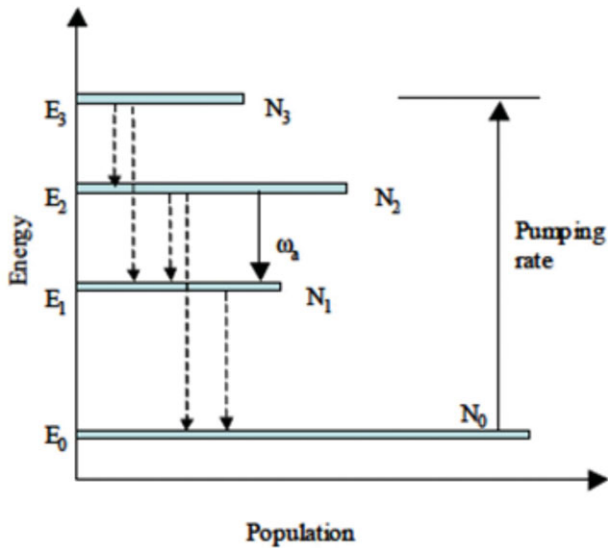


Figure 2 Schematic view of an effective four-level atomic system to model the dynamics of active materials.

($i = 0, 1, 2, 3$) for different atomic levels, as shown in Fig. 2. The total electron concentration $N_{\text{tot}} = N_0 + N_1 + N_2 + N_3$ is a constant determined from realistic materials. An external mechanism pumps electrons from the ground-state level N_0 to the third level N_3 at a certain pumping rate Γ_{pump} , which is proportional to the optical pumping intensity in the experiments. After a short lifetime τ_{32} , electrons transfer nonradiatively into the metastable second level N_2 . The second level E_2 and the first level E_1 are called the upper and lower lasing levels and electrons can be transferred from the upper to the lower lasing levels by spontaneous and stimulated emission. Finally, electrons transfer quickly and nonradiatively from the first level N_1 to the ground-state level N_0 . The lifetimes and energies of the upper and lower lasing levels are τ_{21}, E_2 and τ_{10}, E_1 , respectively. By incorporating the energy transfer between the atoms and electromagnetic fields, the dynamics of occupation numbers of the atoms can be described by the four-level rate equation [64, 65]:

$$\begin{aligned} \frac{dN_3(t)}{dt} &= -\frac{N_3(t)}{\tau_{32}} + \Gamma_{\text{pump}}N_0 \\ \frac{dN_2(t)}{dt} &= \frac{N_3(t)}{\tau_{32}} - \frac{N_2(t)}{\tau_{21}} + \frac{1}{\hbar\omega_a}E(t) \cdot \frac{dP(t)}{dt} \\ \frac{dN_1(t)}{dt} &= \frac{N_2(t)}{\tau_{21}} - \frac{N_1(t)}{\tau_{10}} - \frac{1}{\hbar\omega_a}E(t) \cdot \frac{dP(t)}{dt}, \\ \frac{dN_0(t)}{dt} &= -\frac{N_1(t)}{\tau_{10}} - \Gamma_{\text{pump}}N_0 \end{aligned} \quad (2)$$

where ω_a is the central frequency of radiation of the materials related to the atomic transition energy levels through $\omega_a = (E_2 - E_1)/\hbar$ and $(\hbar\omega)^{-1}E(t)dp(t)/dt$ is the induced radiation rate or excitation rate depending on its sign.

Based on the classical electron oscillator model, the net macroscopic polarization $P(t)$ induced in the presence of an applied electric field $E(t)$ for an isotropic medium can be

described as follows [66]:

$$\frac{d^2P(t)}{dt^2} + \Delta\omega_a \frac{dP(t)}{dt} + \omega_a^2P(t) = \kappa \Delta N_{12}E(t), \quad (3)$$

where $\Delta\omega_a$ is the line width of the atomic transition, $\Delta N_{12}(t) = N_1(t) - N_2(t)$ is the population inversion that drives the polarization, and κ is the coupling strength of $P(t)$ to external electrical fields. It is known from Eq. (4) that the amplification line shape is Lorentzian and homogeneously broadened.

This self-consistent model can be applied to the study of light amplification, enhanced spontaneous emission, and even lasing action in systems with active media. Hence, numerical investigation of the optical properties of microtubes with gain by this model may uncover new interesting optical phenomena to benefit experimental investigations.

2.2. Finite-element method

The finite-element method (FEM) is a versatile numerical technique in electromagnetic computation [67–69] and is capable of handling arbitrary shapes and different materials. FEM is based on subdividing the computational domain into smaller subdomains called finite elements and expressing Maxwell's equations under the associated boundary conditions as a set of linear equations that can be solved computationally using linear algebra. The finite elements can be nonorthogonal polyhedra with triangular, quadrangle or curved shapes in two dimensions. To simulate microtubes by FEM, the computational domain, the geometry of the structure, grids, and boundary conditions should be taken into consideration, similar to the procedures in the FDTD method. However, unlike FDTD simulation, which is restricted to the time domain, FEM can be performed in both the frequency and time domains. While optical resonances in microtubes can be investigated directly in the frequency domain, propagation of light in microtubes can be tracked in the time domain.

FEM has two advantages over the FDTD method. The first advantage is that nonuniform spatial and nonorthogonal grids are used to discretize the computational domain in FEM. This is essential when dealing with systems that consist of objects with characteristic lengths different from each other and having curved boundaries. As a demonstration, we consider a microtube with a single-layered wall in a dielectric matrix as shown in Fig. 3. In order to resolve the geometric details of the wall, finer grids are used in the wall region, whereas coarser grids are employed in other regions. The second advantage is that arbitrary materials parameters can be adopted. Modeling materials with exotic parameters, for instance, metamaterials with extreme anisotropy, is a great challenge. It has been shown that they can be handled reliably by FEM. Smith et al. have investigated the optical properties of microtubes with multilayered walls consisting of alternative dielectric and metallic layers [70] and these microtubes can be regarded as ones with single-layered walls composed of anisotropic

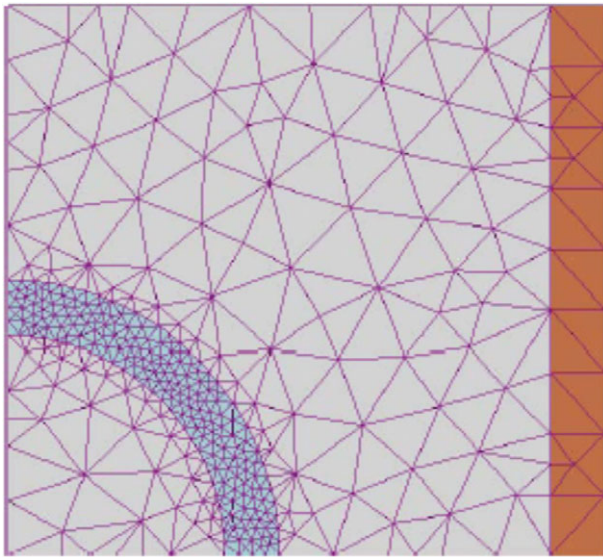


Figure 3 Schematic diagram of discretization of computational domain in FEM simulation.

materials. However, FEM demands more computational resources such as time and memory than FDTD. For example, assuming the scale of the system is N , the computational effect in FEM is N^2 since linear equations are involved in FEM, whereas it is N in FDTD.

2.3. Boundary-element method

The boundary-element method (BEM) is a numerical method used to solve linear partial differential equations (PDE) formulated as integral equations (i.e. in the boundary integral form) [71]. It can be applied to fluid mechanics, acoustics, and electromagnetics, and fracture mechanics. In electromagnetics, the more traditional term is “method of moments”. The essential reformulation of PDEs that underlies BEM consists of an integral equation defined by the boundary of the domain and an integral that relates the boundary solution to the solution at points in the domain. The former is termed a boundary integral equation (BIE) and BEM is often referred to as the boundary integral equation method or boundary integral method.

BEM is often more efficient than FEM and FDTD in terms of computational resources when addressing situations related to a small surface/volume ratio. The advantage of BEM is that only the boundary (or boundaries) of the domain of the PDE requires subdivision, whereas in FEM or FDTD, the whole domain of the PDE requires discretization. Hence, the dimension of the problem is effectively reduced by one. For example, an equation governing a 3D region is transformed into one pertaining to the surface. In cases where the domain is exterior to the boundary, the extent of the domain is infinite and hence, BEM is even more advantageous and the equation governing the infinite domain is reduced to an equation over the (finite) boundary.

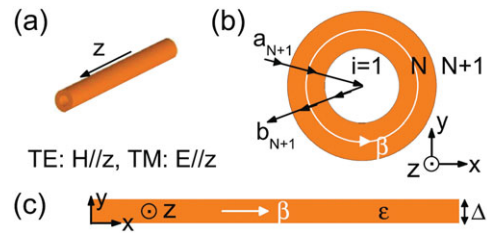


Figure 4 Schematic diagrams: (a, b) An N -layered cylindrical structure [$N=2$ is shown] and (c) Flat dielectric film with dielectric constant ϵ and thickness Δ in air [72].

BEM is applicable to problems in which Green’s functions can be calculated, thus usually involving linear homogeneous media. This places considerable restrictions on the range and generality of problems to which boundary elements can be applied.

2.4. Mie scattering method

When the wall thickness of microtubes is smaller than the wavelength range of interest, it is reasonable to neglect the structural imperfections in the microtubes such as lobes on the inside and outside rolling edge and possible defects. This approximation can serve as a good starting point for analytical investigation of optical properties of microtubes [48, 63, 72]. The microtube can be treated as an N -layered cylindrical structure as shown in Figs. 4a and b. The wall of the microtube is a film with $N-1$ layers and the layer index i of the core and background are 1 and $N+1$, respectively. The i th layer has an outer radius of r_i and dielectric constant of $\epsilon_i \equiv n_i^2$ and the microtube is along the z direction. We consider transverse-magnetic (TM)/transverse-electric (TE) waves that are propagating in the x - y plane with the electric/magnetic field along the z direction.

The Mie scattering method can be applied to investigate the optical response of microtubes. When TM (TE) waves impact a microtube, the electric field $E_z(r, \phi)$ (magnetic field $H_z(r, \phi)$ in the i th layer) can be expressed as [72]

$$\Psi_i(r) = \sum_m [a_{i,m} J_m(k_i r) + b_{i,m} H_m^{(1)}(k_i r)] e^{im\phi}, \quad (4)$$

where Ψ represents E_z (H_z) of the TE (TM) waves, $k_i = \sqrt{\epsilon_i} k_0$. The origin of the cylindrical coordinates (r, ϕ) is at the center of microtube and the Bessel function J_m and Hankel function $H_m^{(1)}$ of the first kind stand for the incident and scattering waves, respectively. Using continuities of E_z (H_z) and $\frac{\partial}{\partial r} E_z$ ($\frac{1}{\epsilon} \frac{\partial}{\partial r} H_z$) for TM (TE) waves, we have

$$\frac{J'_m(u) + D_{i+1,m} H_m^{(1)'}(u)}{J_m(u) + D_{i+1,m} H_m^{(1)}(u)} = \frac{\alpha_i J'_m(v) + D_{i,m} H_m^{(1)'}(v)}{\alpha_{i+1} J_m(v) + D_{i,m} H_m^{(1)}(v)}, \quad (5)$$

where $u = k_{i+1}r_{i+1}$, $v = k_i r_{i+1}$, $D_{i,m} \equiv b_{i,m}/a_{i,m}$, and $\alpha_i = k_i(k_i \varepsilon_i)$ are for the TM (TE) waves [72]. Using $D_{1,m} = 0$ and Eq. (1), we can obtain the scattering coefficient $D_{N+1,m}$ of the microtube. The total scattering cross section of the microtube is obtained by the following relationship [73, 74]:

$$C_s \equiv \sum_m C_{s,m} = \sum_m \frac{2\lambda}{\pi} |D_{N+1,m}|^2. \quad (6)$$

Near the resonant wavelength λ_m , the partial scattering cross section has a Lorentz line shape [74, 75], $C_{s,m} = 4k_0^{-1} \gamma_m^2 / [(k_0 - k_m)^2 + \gamma_m^2]$, where $k_m = 2\pi/\lambda_m$ and λ_m is the resonant wavelength. The Q-factor of the m th-order resonance can be obtained by $Q = k_m/(2\gamma_m)$. The resonant wavelength and Q-factor can also be obtained by identifying the pole of the scattering cross section in the complex-frequency plane. However, the calculation is more time consuming and the underlying physics is more complex.

It should be mentioned that the resonant wavelength of the microtubes can be estimated by regarding the microtube wall as a rolled-up planar waveguide with an effective dielectric constant ε and thickness Δ . The waveguide modes in the planar waveguide are described by the propagating constant β that can be obtained analytically by applying the whispering gallery conditions $\beta L = 2\pi m$, where $L = \pi(r_1 + r_N)$ and that the integer m is the order of resonance. The results obtained from this waveguide approximation method agree well with those by the rigorous Mie scattering method when the optical thickness of waveguide ($\sqrt{\varepsilon}\Delta$) is sufficiently small with respect to the resonant wavelength.

2.5. Adiabatic approximation for axial confinement

Structural variations along the axial length of the microtube can change the axial field distribution and lead to axially confined modes oscillating back and forth along the axis. Under the conditions that the cylindrical symmetry of the microtube with respect to its axis remains and there are few variations of the tube diameter along the axial length, these axially confined modes can be treated by adiabatically separating the azimuthal and axial modes, as proposed by Kipp and coworkers [48, 76]. Starting from Maxwell's equation for TM waves:

$$-\frac{1}{n(r, \theta, z)^2} \nabla^2 E_z(r, \theta, z) = k_0^2 E_z(r, \theta, z), \quad (7)$$

where k_0 is the wave number in air and $n(r, \theta, z)$ is the refractive index profile of the microtube. The tube axis is assumed to be along the z direction. The solution of Eq. (7) has the form:

$$E_z(r, \theta, z) = \sum_m a_m \Phi_m(r, \theta; z) \Psi_m(z), \quad (8)$$

where $\Phi_m(r, \theta; z)$ is the solution of circulating propagation at a fixed z , m is the angular index, a_m is the expansion coefficient, and $\Psi(z)$ is the envelope of the solution along the axial length. $\Phi_m(r, \theta; z)$ satisfies the two-dimensional scalar wave equation:

$$-\frac{1}{n(r, \theta; z)^2} \nabla^2 \Phi_m(r, \theta; z) = k_c^2 \Phi_m(r, \theta; z), \quad (9)$$

where k_c is the wave number of the circulating propagation. $\Phi_m(r, \theta; z)$ is normalized to

$$\langle \Phi_m | \Phi_m \rangle = 1, \text{ where } \langle \parallel \rangle = \int \int dr d\theta.$$

Substituting Eq. (9) into Eq. (8), we obtain:

$$\begin{aligned} & -\frac{1}{n^2} \sum_m a_m [\nabla_{r,\theta}^2 \Phi_m \Psi_m(z) + \Phi_m \nabla_r^2 \Psi_m(z)] \\ & = k_0^2 \sum_m a_m \Phi_m \Psi_m. \end{aligned} \quad (10)$$

Multiplying Eq. (10) by $\Phi_m^*(r, \theta; z)$ and integrating over the cross section of the microtube on both sides using Eq. (6), it becomes:

$$\begin{aligned} & -\frac{1}{n^2} a_m (k_c^2 \Psi_m - \frac{1}{n_c^2} \nabla_z^2 \Psi_m) \\ & + \sum_{p \neq m} a_p (k_{pm}^2 \Psi_p - \frac{1}{n_{pm}^2} \nabla_z^2 \Psi_p) = a_m \Psi_m, \end{aligned} \quad (11)$$

where

$$\begin{aligned} \frac{1}{n_c^2(z)} &= \left\langle \Phi_m \left| \frac{1}{n^2} \right| \Phi_m \right\rangle, \\ k_{pm}^2(z) &= \left\langle \Phi_m \left| -\frac{1}{n^2} \nabla_{r,\theta}^2 \right| \Phi_p \right\rangle, \\ \frac{1}{n_{pm}^2(z)} &= \left\langle \Phi_m \left| -\frac{1}{n^2} \right| \Phi_p \right\rangle. \end{aligned} \quad (12)$$

When the structural variation of the microtube is very slow, we have

$$k_{pm}^2/k_c^2 \ll 1, n_c^2/n_{pm}^2 \ll 1. \quad (13)$$

Under these conditions, Eq. (11) is reduced to the final axial equation:

$$-\frac{1}{n_c^2} \nabla_z^2 \Psi + k_c^2 \Psi = k_0^2 \Psi. \quad (14)$$

Equation (14) resembles the 1D Schrödinger equation for a particle moving in an effective potential defined by k_c^2 and n_c can be regarded as the effective mass of the particle. In simple cases, for example, when n_c is a constant and $k_c^2 \propto z^2$ and taking the form of a harmonic potential, Eq. (14) can be

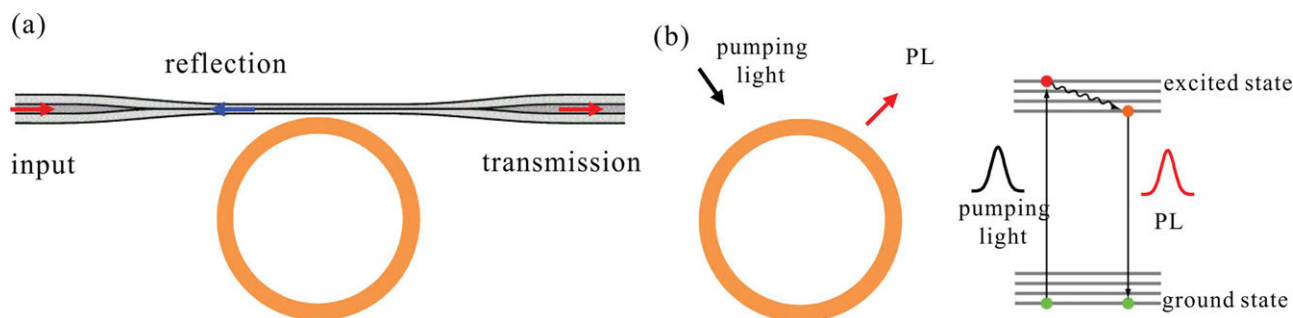


Figure 5 Schematic diagrams for the coupling of light into tubular cavities based on (a) fiber evanescent coupling and (b) photoluminescence (PL) effects of the microcavity. In (a), when light propagates in an optical fiber, it can couple to the cavity through an evanescent field. In (b), the wall of the cavity consists of a photoluminescent material with its electronic structure shown schematically in the right panel. Resonance modes of the system can be excited by using the pumping light.

solved analytically to yield the energy spectrum of a simple harmonic oscillator. On the other hand, the energy spectrum and axial modes profile in general cases can be obtained by numerically solving Eq. (14) by the finite-difference method.

It should be noted that n_c can vary along the axial length of the microtube. According to Eq. (12), n_c is the weighted average of the refractive index over the cross section of the microtube (including its environment and core). The weighting factor is determined by the intensity profile of the corresponding azimuthal modes. With respect to resonant modes with high Q-factors, the mode profiles concentrate within the tube wall and n_c can be approximately taken as the average value of the refractive index of the tube wall. However, for those with low Q-factors, the fields can penetrate considerably into the environment and core and hence, n_c may exhibit remarkable changes along the axis of the microtube.

By fabricating microtubes with a variety of axial profiles, researchers have systematically investigated the effects of different axial potentials on the properties of resonant modes of the microtubes. The Q-factors and axial confinement of the resonant modes can be tailored with different axial potentials and so it is also possible to change the effective mass n_c to tailor the optical properties of resonant modes in order to uncover new phenomena.

All the methods mentioned above have their own characteristics and several methods can be used in conjunction to solve a problem. The perturbation theory is quite effective and suitable for the calculation of defects in microcavities or nanoparticles on the surface of tubular microcavities [77–79]. Both the Mie scattering theory and adiabatic approximation have been employed to determine the optical axial confinement [72] and more details concerning 3D optical confinement can be found later in Section 4.

3. Light propagation in microtubular cavities

The optical properties of microtubular cavities such as the Q-factor, polarization, and 3D optical confinement play important roles in optical devices in microsystems or lab-on-

a-chip systems. To experimentally investigate the optical properties of tubular cavities, it is of great importance to achieve efficient coupling of light into the system. Two schemes based on fiber evanescent coupling and photoluminescence (PL) effects of the cavities respectively are mainly used, as shown in Fig. 5. For the former one, consider placing an optical fiber in close proximity to tubular cavities. When light propagates in the fiber, it can couple into the cavities through an evanescent field. Optical resonances in the cavities can be detected by transmission (reflection) spectra through (from) the fiber. This coupling scheme allows for highly efficient and mode-selective coupling. However, due to the strong coupling between cavities and fiber, Q-factors of resonances in the cavities can be decreased remarkably. For the latter one, by incorporating photoluminescent materials into the walls of tubular cavities, resonance modes with high Q-factors can be excited by using pumping light. Optical resonances are probed from PL spectra. Note that the Q-factors of resonances will not be altered in this scheme. However, all resonance modes with frequencies inside the spectral range of PL emission can be excited, while their intensity mainly depends on their Q-factor, respectively. In this section, some traditional and important physical properties are introduced to reveal their superior characteristics in the field of label-free (bio-)chemsensors.

3.1. Evanescent wave

When a light beam is totally internally reflected on a dielectric interface separating an optically high-index medium and optically lower-index medium, the reflected light beam is slightly shifted compared to the one in the classical approach using geometrical optics. This phenomenon is known as the Goos–Hänche effect [80]. The Goos–Hänche shift (GHS) is a lateral shift of totally reflected beams along the optical interface. That is, the points of incidence and reflection do not coincide. This is attributed to the phase changes due to the evanescent wave that propagates into the lower-index medium near the interface [81]. In this case, the beam appears to travel as an evanescent wave over a short distance through the optically low-index

medium. Thus, in each reflection along the circular path of WGMs, the light seeps into the surroundings as an evanescent wave [2–4, 9, 54, 82–87]. A larger GHS corresponds to a larger evanescent wave as it propagates into the lower-index medium near the interface. The characteristics and theoretical simulation of GHS and evanescent wave are still actively investigated [88–91] although they are sometimes ignored because the exponentially small magnitude is far below that of the refracted field. However, the evanescent wave plays an important role in optical microcavities with a tubular geometry and thin walls (several micrometers or subwavelength thick). Most of optical properties in microcavities show a strong relationship with the evanescent wave and it will be discussed in the following sections. To demonstrate the relationship between the optical properties of tubular microcavities and evanescent wave, the influence of polarization state and wavelength of incident light wave on the evanescent wave is first discussed.

The GHS can be different if the polarization state of the incident light wave is changed. The optical-beam displacements in the incident plane are not the same for TE-polarized wave (the electric vector parallel to the incident plane) and TM-polarized wave (the electric vector perpendicular to the plane of incidence). The difference between the GHS reaches a maximum between TE- and TM-polarized waves with the same wavelength [91]. The polarization-dependent GHS phenomena are confirmed by experiments and theoretical simulation [91] and the penetration depth is larger in the TE mode (s polarization) than the TM mode (p polarization) [80, 81, 92]. It should be noted that the definition of TE and TM mode (polarization) is under debate. The details will be discussed in Section 3.3 with Figs. 4 and 10. To compare the experimental data with theory, the GHS versus the incident angle relationship is derived numerically using Artmann's formulas [93]:

$$d_{\text{TM}} = \frac{\lambda}{\pi} \frac{\sin(i)}{[n^2 \sin^2(i) - 1]^{1/2}} \quad (15)$$

$$d_{\text{TE}} = \frac{d_{\text{TM}}}{[(1 + n^2) \sin^2(i) - 1]^{1/2}}, \quad (16)$$

where $d_{\text{TE (TM)}}$ represents the GHS for the TE (TM) eigenstate, i is the incident angle on the plane dielectric surface, and n is the refractive index.

The difference between the TE and TM longitudinal GHS versus the angle of incidence at $\lambda = 0.67 \mu\text{m}$ ($n = 1.511$, circle and solid line) and $\lambda = 1.083 \mu\text{m}$ ($n = 1.506$, cubic and break line) are shown in Fig. 6. The relative sign of the two signals is to ensure that the TE polarization state is characterized by a higher displacement than the TM state. The TE mode thus suffers a larger optical loss than the TM mode at the surface of the optical microcavities, where the evanescent wave is possibly coupled with the radiation mode or absorbed slightly by the surrounding low-index media (Fig. 6). Figure 6 indicates that the agreement between the experimental measurements and theoretical calculation is good [91]. Furthermore, the GHS is proportional to the incident light wavelength [91]. In

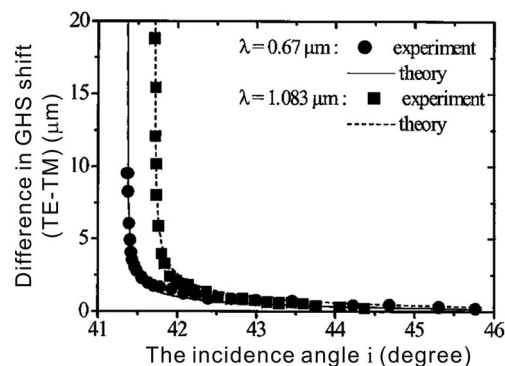


Figure 6 Difference between the TE and TM longitudinal GHS versus the angle of incidence at $\lambda = 0.67 \mu\text{m}$ ($n = 1.511$, circle and solid line) and $\lambda = 1.083 \mu\text{m}$ ($n = 1.506$, cubic and break line), respectively. Reproduced with permission from ref. 91 (the polarization states are redefined in this review).

the short-wavelength limit $\lambda \rightarrow 0$, the GHS disappears, leading to the standard ray dynamics of geometric optics and the displacement of TM (or TE) polarization increases with incident wavelength (Fig. 6). Consequently, the evanescent wave increases with increasing incident wavelengths.

This difference in the optical loss caused by the evanescent wave is thought to affect the polarization characteristics, Q-factor, and sensitivity of tubular optical microcavities [92]. The light wavelengths in WGMs microresonators are confined by continuous total internal reflection. In each reflection along the circular path of WGMs, the light seeps into the surroundings as an evanescent wave [2–4, 9, 54, 82–87]. Based on the discussion on the GHS and evanescent wave, two points are noted. First, the TE mode shows a larger light loss in each reflection along the circular path of the tubular WGMs microresonators than the TM mode. And secondly, the light loss in the tubular WGMs microresonator increases with the light wavelength.

The evanescent waves affect the properties of optical microcavities such as the Q-factor and polarization and the application of microcavities is also greatly influenced by the evanescent waves. At the same time, the evanescent waves are used to characterize the optical properties of optical microcavities and fabricate new optical devices. These issues will be discussed in detail later in this review.

3.2. Q-factor dependence on tubular wall characteristics

Among the various important characteristics of optical microresonators, the Q-factor is one of most basic parameters. It is a measure of the energy loss and defined by the time-averaged energy in the cavity divided by the energy loss per cycle [33]:

$$Q = \omega \frac{\text{Stored energy}}{\text{Power loss}}. \quad (17)$$

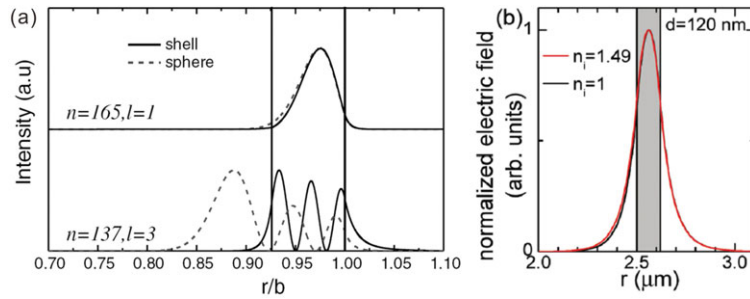


Figure 7 (a) Calculated angle-averaged radial distribution of $TE_{165,1}$ and $TE_{137,3}$ in a homogeneous sphere and a shell for $a = 0.926b$ (inner radius $a \sim 11.9 \mu\text{m}$ and outer radius $b \sim 12.8 \mu\text{m}$) [103]. (b) Radial field distribution calculated for a ring with the diameter of the self-rolled tube and a wall thickness of 120 nm. The refractive index of the tube wall (gray shaded region) is assumed to be 3.3. Outside the tube we set $n = 1$. For the red (black) curve a refractive index inside the tube of $\eta_1 = 1.49$ for toluene ($\eta_1 = 1$ for vacuum) is used [85].

The Q-factor in a resonant mode is an estimation of the finite photon lifetime in practice and can be determined by the ratio of the resonant frequency and the full width at half-maximum (FWHM) bandwidth of the resonance peak. In order to characterize the property of a resonator by keeping its energy inside for a decay time τ , Q-factor can also be expressed as [12, 33]:

$$Q = \frac{\omega}{\Delta\omega} = \omega\tau, \quad (18)$$

where $\Delta\omega$ is the linewidth (FWHM) of the Lorentzian peak associated with the considered resonance. The Q-factor of the WGM is determined by other mechanisms that cause light losses in WGMs. Thus, it is convenient to introduce the partial Q-factors Q_j related to each type of light losses in the microcavities and to describe Q by the well-known expression $Q = \sum_j Q_j$ [12, 94, 95].

Normally, in an isolated (not coupled) WGM optical microcavity, the overall Q-factor (the intrinsic Q-factor of the resonators) is determined by the individual loss terms according to [12]:

$$Q_0^{-1} = Q_{\text{rad}}^{-1} + Q_{\text{mat}}^{-1} + Q_{\text{s.s}}^{-1} + Q_{\text{cont}}^{-1}. \quad (19)$$

The first term Q_{rad} denotes radiative (curvature) losses. Q_{rad}^{-1} vanishes exponentially with increasing size and for resonator diameters larger than $10 \mu\text{m}$ radiative losses are negligible [12, 96]. Q_{mat} is associated with absorption and bulk Rayleigh scattering in the materials constituting the microcavities. $Q_{\text{s.s}}$ denotes scattering losses due to residual surface inhomogeneity. There are many different expressions for $Q_{\text{s.s}}$ [95, 97–100]. Q_{cont} denotes the losses introduced by surface contaminants during the fabrication process. The limitation of the ultimate Q-factor caused by adsorption of atmospheric water on the surface of fused-silica microresonators is demonstrated in 1996 [101] and $Q_{\text{s.s}}$ and Q_{cont} are both defined as $Q_{\text{s.s}}$ (scattering light losses due to surface inhomogeneity).

In WGM microresonators, the most important loss terms are bulk absorption and scattering at surface inhomogeneities [96]:

$$Q_0^{-1} = Q_{\text{mat}}^{-1} + Q_{\text{s.s}}^{-1}. \quad (20)$$

Similarly, in an isolated (not coupled) WGM optical microcavity with a tubular geometry, the overall Q-factor can be

expressed as [94]:

$$Q = Q_{\text{rad}}^{-1} + Q_{\text{wall}}^{-1} + Q_{\text{s.s}}^{-1} \approx Q_{\text{wall}}^{-1} + Q_{\text{s.s}}^{-1}, \quad (21)$$

where Q_{rad} , Q_{wall} , and $Q_{\text{s.s}}$ are the Q-factors that are reasonably determined by the radiation loss, loss in the wall medium, and loss resulting from the surface scattering, respectively [94]. Based on a detailed analysis on the Q-factors of the WGMs, it is noted that all WGMs (up to the 15th order) have $Q_{\text{rad}} \gg 10^{11}$ [94]. Thus, Q_{rad} is negligible. If the WGM optical microcavities with a tubular geometry is filled with liquid, the Q-factor Q_{liq} is determined by [94]:

$$Q_{\text{liq}}^{-1} = Q_{\text{wall}}^{-1} + Q_{\text{s.s}}^{-1} + \eta_1 Q_{\text{sol}}^{-1}. \quad (22)$$

In WGM microresonators with a tubular geometry, the most important light loss terms are light loss in the wall medium (Q_{wall}), scattering at surface inhomogeneity ($Q_{\text{s.s}}$), and light loss caused by the liquid in the tubes core (Q_{sol}), and η_1 is the fraction of evanescent wave light outside the tube wall. The Q-factor increases as η_1 decreases. The influence of wall thickness and materials index, surface roughness, and liquid medium on the Q-factor of WGM optical microcavities with the tubular geometry cannot be overlooked.

Based on Mie scattering theory simulation, the Q-factor of tubular optical microcavities can be increased by increasing the wall thickness and effective index constant [72] and reduced by increasing the wavelength [102] because of the properties of the evanescent waves. The evanescent waves impact the Q-factor significantly.

Figure 7 indicates that light can be confined in the wall of the fiber-drawing glass capillary [103] and self-rolled optical microcavities [85]. Meanwhile, the modes generate outer and inner evanescent wave at the regions $r < a$ (r is the radial position; a is the inner radius) and $r > b$ (b is the outer radius) defined as the inner evanescent wave and outer evanescent wave, respectively. Compared to traditional capillary optical microcavities (Fig. 7a), the evanescent wave fraction of self-rolled optical microcavities with ultrathin wall thickness is higher (Fig. 7b). The Q-factor decreases with larger fraction of evanescent wave. The Q-factor indicates light confinement and the evanescent wave is generally related to light loss. Therefore, the Q-factor of the self-rolled tubular optical microcavities (< 5000) is smaller than that of other types of optical microresonators with a tubular geometry ($> 10^4$). However, the inner

evanescent wave and outer evanescent wave inside and outside the tube are different in tubular optical microcavities. This ensures efficient coupling of the external emitters or analyte with the optical modes and opens up, for example, the possibility of evanescent field-coupled lasing [29] of external emitters in microtube resonators or lab-on-a-chip sensors to detect analytes such as DNA, cells, molecules, proteins, and viruses [13]. Some of these interesting applications will be discussed in Section 5. Three parameters: the wall thickness and morphology, index contrast, and materials in the tube walls influence the Q-factors of tubular optical microcavities and the influence of the wall thickness, materials index, and liquid medium on the Q-factor of WGM optical microcavities with a tubular geometry will be discussed in detail in the following section. The influence of the evanescent wave will also be briefly described.

(1) Wall thickness and morphology

The wall of the tubular optical microcavities supports the WGMs. Owing to the Goos–Hänche effect, in each reflection along the circular path of WGMs, the light seeps into the surroundings as an evanescent wave [2–4, 9, 54, 82–87]. Meanwhile, based on the Mie scattering theory, the Q-factor bears a strong relationship with the wall thickness [104]. In tubular microcavities with the same index constant, the wall thickness and morphology are crucial for achieving (ultra-)high Q-factor. Hollow structures show higher Q-factors than solid structures for spherical microcavities by a factor of about 10 [43]. Figure 7a shows the calculated angle-averaged radial distributions of the two modes ($TE_{165,1}$ and $TE_{137,3}$) for the hollow and solid spheres with the same radius. In the solid case, the radial distributions extends far below the inner boundary ($r = a = 0.926b$) compared to the hollow case. The light is strongly confined within $a < r < b$ in the hollow case [103]. The mode distributes deeper from the outside boundary and the corresponding cavity Q-factor decreases, especially for the higher mode order ($l > 1$). The second (radial) mode order (l) indicates the number of maxima in the radial distribution of the internal electric field [54].

Based on Eq. (22), the Q-factor increases when η_1 (the fraction of evanescent wave light outside the tube wall) decreases. Figure 7 shows that the evanescent wave percentage of the glass capillary with thick wall ($\sim 1 \mu\text{m}$, mode order $l = 1$) is smaller than that of self-rolled microtubes with an ultrathin wall ($\sim 150 \text{ nm}$ thick). In other words, the light loss in a self-rolled tubular optical microresonator is dramatically higher than that in the glass capillary resonator. Hence, compared to glass capillary microcavities with a thick wall ($> 0.5 \mu\text{m}$), the silica glass self-rolled microtubes with an ultrathin wall (subwavelength, $< 150 \text{ nm}$) have a smaller Q-factor (less than 10^3). For one given azimuthal mode (m) of tubular optical microcavities with thick walls (wall thickness/outer diameter > 0.05), the Q-factor increases slightly with wall thicknesses [104], whereas for one given azimuthal mode (m) of tubular optical microcavities with (ultra-)thin walls (wall thickness/outer diameter

< 0.05), the Q-factor increases dramatically with increasing wall thickness [104, 105].

Compared to (ultra-)high Q-factor (higher than 10^4) optical microresonators resembling microspheres, microspheroids, and toroids, the Q-factor of tubular microcavities without coupling is quite small (less than 5000). In some optical microresonators, self-interference can produce a resonant mode that is strongly localized along the axial direction to produce 3D optical confinement, but the WGMs in a uniform long tubular microresonator without taper coupling are delocalized. More details about 3D optical confinement are described in Section 3.4.

(2) Index contrast

Both theoretical simulation and experimental data indicate that high-index materials are good for (ultra-)high Q-factor microcavities. Based on Artmann's formulas (see Section 3.1), the evanescent wave increases with decreasing index contrast between the wall of the microcavity and low-index medium. Hence, the tubular microcavities with a high index contrast wall support low-light-loss WGMs [106, 107], meaning that the high index contrast microcavities possess (ultra-)high Q-factors compared to the low index contrast ones. Both the ultrathin wall (subwavelength) and effective index constant of the self-rolled microresonator are smaller than those of the glass capillary. The self-rolled optical microcavities with (ultra-)thin walls show small light confinement in the microcavities. Therefore, it is reasonable that the Q-factor (less than 5000) of a self-rolled microtube with ultrathin wall is still smaller than the Q-factor (larger than 10^4) of the fiber-drawing glass capillary. Meanwhile, the experimental results and Mie scattering show that the self-rolled microcavities with high effective index possess a high Q-factor compared to those with a low effective index [102]. Furthermore, the main limit of the WGM Q-factor in Eq. (22) is related to the contribution Q_{wall} associated with absorption and bulk Rayleigh scattering in the materials constituting the tubular microcavities. Q_{wall} can be approximated as [12, 108]:

$$Q_{\text{wall}} \propto \frac{2\pi n}{\alpha \lambda}, \quad (23)$$

where λ is the light wavelength in vacuum, α is the absorption coefficient, and n is the refractive index. This approximation shows that the Q-factor increases as the refractive index (n) increases. As the index constant of the semiconductor ($n > 3$) is higher than that of silica ($n \sim 1.5$), the Q-factor of InGaAs/GaAs rolled-up microtube laser (~ 3500) [58, 109] is higher than that of SiO/SiO₂ bilayer self-rolled tubular microcavities without a coating (Q-factor less than 1000) [34].

High index contrast microcavities support low-loss WGMs [106]. In order to optimize the optical properties of tubular microcavities, two processes can be adopted, (1) choosing high index constant materials: Y₂O₃/ZrO₂ self-rolled microcavities without surface modification with larger Q-factors (> 1500) than SiO/SiO₂ [102] and

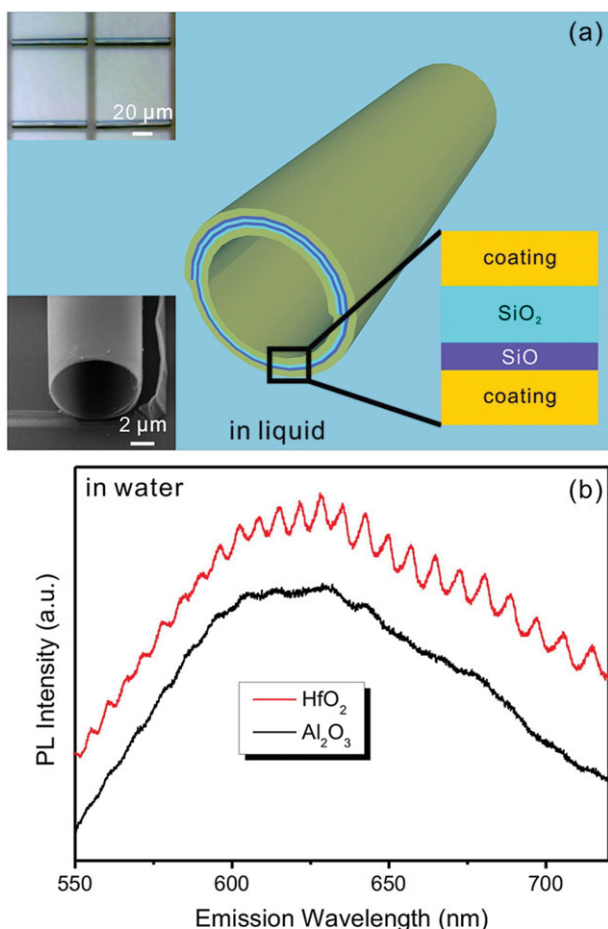


Figure 8 (a) 3D schematic diagram of a rolled-up nanomembrane in liquid. The bottom-right inset illustrates the multilayered structure of the wall, the top-left inset shows an optical microscope image of an ordered array of rolled-up nanomembranes, and the bottom-left inset shows a bird's-eye view SEM image of the opening of a rolled-up nanomembrane. (b) Photoluminescence (PL) spectra obtained in water from rolled-up nanomembranes with HfO_2 and Al_2O_3 coating layers (30 nm thick in both cases) taken under excitation of the 442-nm line of a He-Cd laser [9].

(2) coating the tube walls with high index constant materials. When the self-rolled optical microcavities are coated with the same thickness materials with different indexes, the high index coating will effectively enhance the Q-factor. For example, Fig. 8 indicates that HfO_2 effectively improves light confinement compared to the Al_2O_3 coating since HfO_2 has a larger refractive index [9].

Besides the diameter of optical microcavities (see Section 3.4), the same effect can be achieved by creating an “index bottle” without involving any diameter change along the axial direction [110]. These prolate “index bottle” WGM microcavities possess ultralarge Q-factors of 2×10^5 [110].

(3) Inside and outside medium

The main limit of the WGM Q-factor in Eq. (22) is related to the contribution Q_{sol} associated with light loss caused by the liquid in the tube core [94]. The wall of the tubular optical microcavities supports WGMs and the evanescent wave interacts with the inside and outside surrounding medium when the evanescent wave light seeps into the surrounding medium [9, 85, 94, 111–113]. Based on Eq. (21), the Q-factor increases as η_1 (the fraction of evanescent wave light outside the tube wall) decreases. The Q-factor is influenced by the inside and outside liquid media and here, both experimental and theoretical results are discussed.

The liquid index influences the self-rolled-up optical microcavities with subwavelength wall thickness as observed by Huang et al. [9] and Moon et al. [103]. Huang et al. noticed that as the refractive indices of the surrounding media increased, light loss for WGMs modes increased and the Q-factor of the WGMs in the tubular optical microcavities decreased. However, light loss in the TE modes was much more prominent than in the TM modes, rendering the TE modes undetectable in liquids [9]. The Q-factors of big microcavities (the diameter is around 9 μm) in air and liquid are ~ 480 and ~ 220 , respectively, for the mode at ~ 2 eV, and those of the small microcavity (the diameter is around 7 μm) are ~ 660 and ~ 250 , respectively [9]. Moon et al.'s results indicate the Q-factor of glass capillary microcavities increases as the refractive index of the inner region increases [103]. As the liquid index increases from 1.0 to 1.1 and 1.15, the Q-factor of $\text{TE}_{137,3}$ increases from 4.9×10^3 to 9.0×10^3 and 1.5×10^4 , respectively [103]. The experimental results are consistent with theoretical simulation [104].

Based on Mie scattering theory, a theoretical demonstration about the influence of the liquid medium on the rolled-up tubular optical microcavities was reported by Zhao et al. [104]. Figure 9a shows the cross-sectional schematic view of a microtube. The microtube is placed in four different surroundings: air (Fig. 9d), with a liquid inside and air outside (Fig. 9e), with a liquid outside and air inside (Fig. 9f), and in a liquid (Fig. 9g). The liquid has a refractive index of n_L . The Q-factors of the ideal microtubes depend on the index n_3 of the outer medium (Fig. 9b). For the ideal microtubes with a given diameter, the Q-factor increases with wall thicknesses ($\Delta/h < 0.05$). When Δ/h is smaller than 0.05, the increase in the Q-factor is negligible. When the microtube is surrounded by liquid ($n_L > 1$) on the outside, the index contrast between the microtube wall and liquid is smaller than the index contrast between the microtube wall and air. Under these conditions (Figs. 9f and g), the optical loss caused by the evanescent wave is larger than those under the other two conditions. Thus, for the ideal tubular optical microcavities with (ultra-)thin wall, the Q-factors depend on the index n_3 of the liquid medium. The liquid media inside and outside the microtube result in light loss.

The above studies are performed on ideal microtubes with Q-factors of Q_i . Actually, the fabrication process also

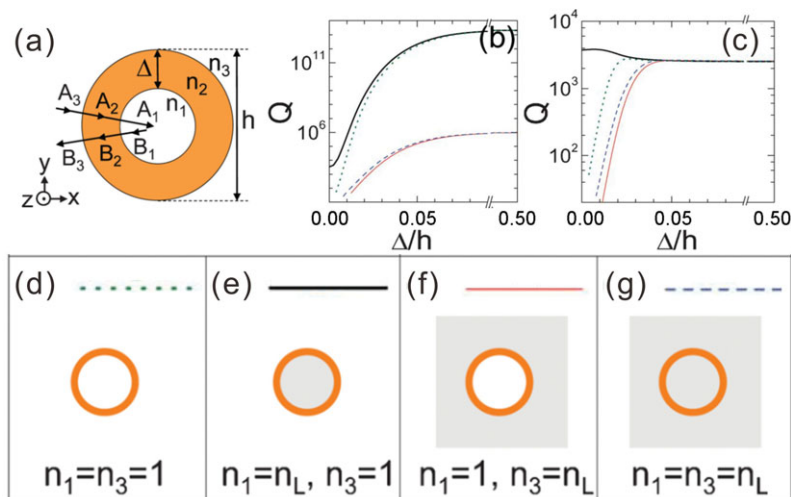


Figure 9 (a) Cross-sectional schematic views of a microtube. The microtube has a diameter of h , wall thickness of Δ and refractive index of n_2 in the wall. The refractive indices are n_1 and n_3 for media inside and outside the microtube, respectively. The incident light propagates in the x - y plane and has E field along the z direction. (b) Q-factors for the $m = 40$ resonant modes of the microtubes in (c)–(f) with $n_2 = 2$ in the tube walls. (c) Q-factors for the $m = 40$ resonant modes of the microtubes in (c)–(f) with $n_2 = 2 + 0.004i$ in tube walls. (d)–(g) The microtube is placed in four kinds of environment: (d) in air (green line in b and c), (e) with liquid inside and air outside (black line in b and c), (f) with liquid outside and air inside (red line in b and c), and (g) in liquid (blue line in b and c). The liquid has a refractive index of n_L [104].

introduces surface imperfections. In rolled-up microtubes, the Q-factor $Q_0^{-1} = Q_i^{-1} + Q_{s,s}^{-1}$, where $Q_{s,s}$ is related to the loss from surface imperfection and cone effects ($Q < Q_i$, $Q_{s,s}$ and $Q_{s,s} < 5000$ in rolled-up microtubes). The diameters of rolled-up tubes vary linearly along the tube axis, which is called the cone effect. As shown in Fig. 9c, we simulate the imperfect microtubes by using a complex refractive index $n_2 = 2 + 0.004i$ in the tube walls. For the tubular optical microcavities with thick walls ($\Delta/h > 0.05$), under all four conditions, the surface imperfections ($Q_{s,s}$) are the main limit of the WGM Q-factors with values smaller than 2000 (Fig. 9c). In the tubular optical microcavities with (ultra-)thin walls ($\Delta/h < 0.05$), the liquid medium influences the surface imperfections more (Fig. 9c). Compared to the tube in air (Fig. 9c, green line), the inside and outside liquid media ($n_L > 1$) lead to light loss and dramatically decrease the Q-factors (black, red, and blue lines in Fig. 9c).

The experimental and theoretical demonstration inside and outside the liquid medium indicate that the Q-factor is reduced by the liquid medium surrounding the tube microcavities with (ultra-)thin walls ($\Delta/h < 0.05$). In optical microcavities with thick walls ($\Delta/h > 0.05$), the influence of surface imperfections is more substantial than that of the elements.

The interaction between the evanescent wave (WGMs) and surrounding media can be used to modify the optical microcavities. Dye-doped optical-gain media have been chosen in microlaser design since 1970s [39, 114, 115]. Various polymeric materials such as PMMA [84, 116], polystyrene (PS) [7], polyurethane (PU) [115], poly(*p*-phenylene-vinylene) (PPV) [25, 117, 118], and poly(1-vinyl-2-pyrrolidone) (PVP) can be used and the main dyes include Rh 6G [84], and pyromethene [7].

The tubular geometry is suitable to contain dye solutions liquid as the gain medium. Compared to the solid gain medium, liquid dye solutions lead to more applications as they can be used as carriers of dyes [40, 86, 87, 92] and luminescent quantum dots [31, 70, 85, 119–123] to introduce special optical properties.

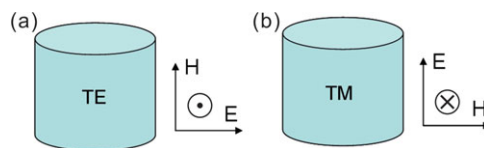


Figure 10 Schematic of TE and TM modes in the optical micro-tubular resonator.

3.3. Polarization of resonant light

Generally, the spectrum of tubular optical microcavities is split into two well-known polarization modes, the transverse-electric (TE) mode and transverse-magnetic (TM) mode defined by the orientation of electric and magnetic fields. However, the definitions of TM polarized and TE polarized vary. In some references, the TM-polarized wave has the electric vector parallel to the incident plane (namely $\vec{r} \cdot \vec{E} = 0$), whereas a TE-polarized wave has the electric vector perpendicular to the plane of incidence (namely $\vec{r} \cdot \vec{E} = 0$) [91, 92, 95]. In other references, the orientation of the electric field of a TE-polarized wave is parallel to the incident plane but that of the magnetic field of a TM-polarized wave is parallel to the incident plane [124]. In the TE mode, the electric field is tangential to the microcavity surface whereas in the TM mode, its electric field is normal to the microcavity surface [9, 72, 104, 125]. In this review, the following polarization definitions are adopted: TE modes with the magnetic field vector parallel to the tube axis and TM modes with the electric field vector parallel to the tube axis (Fig. 10) [9].

The Q-factors bear a strong relationship to the polarization states. Based on Mie scattering theory, compared to the TE modes, the TM modes show larger decay in air [72]. Hence, TM modes are used in experiments and sensors because they have larger Q-factors than the TE modes normally [47, 54, 121, 126]. Another possible reason for the polarization dependence is the mode-field expansion, i.e. the penetration depth of the light wave in the total internal

reflection process [91]. The penetration depth or the GHS (Section 3.1), which is induced by the phase shift on reflection, is larger in the TE mode (p polarization) than TM mode (s polarization) [91]. Hence, the TE mode suffers a larger optical loss at the interface, where the evanescent wave is possibly coupled with the radiation mode or absorbed slightly by the surrounding medium [91]. The difference in the optical loss is thought to affect the polarization characteristics.

The detection sensitivity of optical microcavities changes according to the polarization states. The TE modes exhibit higher sensitivity when the surrounding medium is changed compared to the TM modes [2]. If the Q-factor is not very important, it is better to use the TE modes because the peak shifts are larger than those in the TM modes for the same change in the liquid index constants [2]. Under the same Q-factor condition, the TE modes show higher sensitivities for refractive index detection of the surrounding medium, as verified experimentally [126]. The TM modes of WGMs resonances of capillaries with sub-micrometer wall thickness show a smaller wavelength shift as a function of the refractive index of the medium that fills the interior [126]. The sensitivity of the TM modes (50–70 nm/RIU) is lower than those for the TE modes (130–170 nm/RIU) [126]. Tubes with thin walls are required in order to produce high-sensitivity sensors [126] and the self-rolled optical microresonators have superior performance in this respect [35, 37, 85, 127–129]. The possible reason for this polarization dependence is the evanescent wave. The TE mode has a larger GHS than the TM mode at the interface, where the evanescent wave is possibly coupled with and absorbed slightly by the surrounding medium [91]. Consequently, the TE modes have stronger interaction with the surrounding medium.

The TM modes and TE modes are important to the application of self-rolled optical microcavities [37, 47, 63, 128, 130]. Using the single-scatter-induced coupling mechanism of a pair of counterpropagating high-Q-factor WGMs, the toroidal microcavity can be used to investigate single nonspherical nanoparticles with high sensitivity. The nonspherical particles may produce distinct frequency splitting and additional damping for TE and TM WGMs. This polarization-dependent effect allows the study of the orientation of single biomolecules, molecule–molecule interaction on the microcavity surface, and distinguishing different inner configurations of similar biomolecules [125, 131].

3.4. 3D optical confinement in a geometry-defined tube

Besides the intrinsic evanescent wave in the tubular microcavities, light loss along the axis in the microcavities can degrade the optical properties. Standard WGM microresonators such as dielectric microspheres, microdisks, and microtoroids typically confine the light in a narrow ring along the equator of the structure by continuous total inter-

nal reflection near the resonator surface [3]. These equatorial WGMs have the advantage of an (ultra-)high Q-factor and small mode volume. Contrary to the localized states in the optical spherical/spheroidal and bottle microresonators, the WGMs in a uniform cylindrical or tubular microresonator without microfiber coupling are delocalized. Hence, a circulating light beam in the cylinder eventually radiates outwards along the cylinder axis and opposite to a spherical microresonator, an optical cylinder should not have a large Q-factor.

Two main approaches are employed to improve the optical properties of tubular microcavities. First, when these microcylinder or microcapillary optical microcavities are coupled with microfibers, self-interference of the circulating beam evanescently launched by the microfibers produces the localized state with a simple exponential dependence on the axial coordinates [132a]. Self-interference of the beam in the process of circulation gives rise to a large Q-factor resonant state that is strongly localized along the axial direction. At present, research on applications of microcapillaries with tapered microfiber coupling is quite prevalent. It is noted that light coupling into droplet optical resonators by means of a free-space Gaussian beam (GB) is investigated through numerical simulations and experiments recently [132b]. Furthermore, an enhancement of the cavity finesse Q by a factor of about 10 with respect to CdSe-doped bulk polymer microspheres was found by Artemyev et al. in 2001 [43]. The concept of photons confined in hollow 3D microspheres optical cavities provides a microstructure with large potential to study 3D confined optical modes in the visible spectral range [43]. It is indicated that 3D optical confinement is effective in designing (ultra-)high Q-factor microcavities [43]. Contrary to the 3D optical confinement in optical spherical/spheroidal microresonators, the WGMs in one uniform tubular microcavity without coupling to a microfiber source exhibit smaller Q-factors (10^2 – 10^3). In experiments involving tubular microresonators, full control of the optical modes (with or without fine structure) of the microtube is desirable in order to observe and utilize single, sharp, as well as spatially and energetically well-localized modes and obtain (ultra-)high Q-factors. It is a great challenge to overcome the bottleneck of fabricating special tubular microcavities with 3D optical confinement. In tubular microcavities, a slightly nonuniform and even an ideally uniform optical fiber can perform as well as (ultra-)high Q-factor optical microresonators that have different type of 3D confinement. Several tubular microcavities with 3D optical confinement can be obtained by different methods and here, the basic theory and simulation method of tubular microcavities with 3D optical confinement are discussed in conjunction with experimental verification.

3.4.1. Bottle microresonators

The bottle microresonators are prepared by an improved fiber-drawing process as described in Section 4. Figure 11a

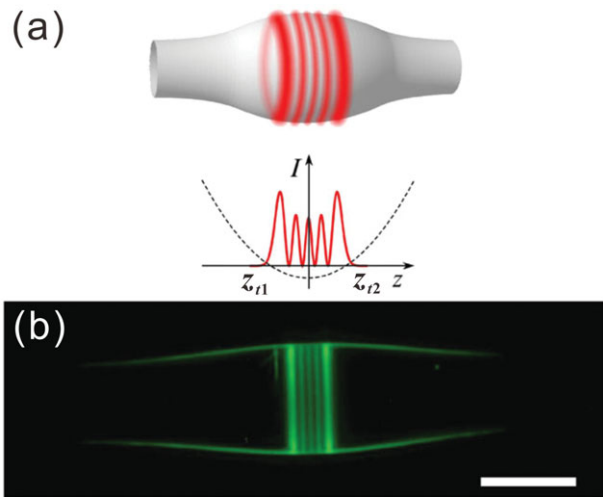


Figure 11 (a) Concept of the bottle microresonator. In addition to the radial confinement by continuous total internal reflection at the resonator surface, the axial confinement of the light is caused by a harmonic effective potential (dashed line) fixed by the curvature of the resonator profile. The resulting intensity distribution is therefore given by the eigenfunctions of the quantum mechanical harmonic oscillator [15]. The intensity is significantly enhanced at the so-called “caustics” of the bottle mode, located at the classical turning points of the harmonic motion. This distinguishing feature gives bottle modes a 3D nature in comparison to equatorial WGMs. (b) Visualizing a $q = 4$ bottle mode in a 36- μm diameter bottle microresonator. The bottle mode is excited by 850 nm laser light and visualized via the upconverted green fluorescence of dopant erbium ions. Scale bar, 30 μm . (adapted from [15])

defines a harmonic effective potential for the light field along the resonator axis. Because of the highly prolate shape, the bottle microresonator gives rise to a class of WGMs with advantageous properties such as ultrahigh Q-factors, microscopic mode volumes, and tunability. The resulting axial standing wave structure exhibits a significantly enhanced intensity at the so-called “caustics” of the bottle mode located at the turning points of the harmonic motion. The 3D optical confinement results from the spiral rays experiencing total internal reflection at the fiber surface and also bouncing along the fiber axis due to reflection from the regions of tapering near the turning points z_{r1} and z_{r2} (Fig. 11a).

The bottle microresonator possesses an equidistant spectrum of eigenmodes labeled by the “azimuthal quantum number” m , which counts the number of wavelengths that fit into the circumference of the resonator and the “axial quantum number” q , which is the number of axial intensity nodes. The radial quantum number p is fixed to its minimum value $p = 1$ corresponding to modes located at the surface of the resonator. As quantum numbers, m , p , and q are integers. According to the semiclassical quantization rule for the bottle eigenstates, Wentzel–Kramers–Brillouin (WKB) quantization along the z -axis produces the equation

that defines the eigenvalues k_{mpq} :

$$\int_{z_{r1}}^{z_{r2}} \left(k_{mpq}^2 - \frac{\mu_{mp}^2}{R(z)^2} \right)^{1/2} dz = \pi \left(q + \frac{1}{2} \right). \quad (24)$$

Here, $R(z)$ is the bottle shape and μ_{mp} depends on the external refractive index and polarization of light. The quantization rules for the bottle states, Eq. (24), can be inverted and thus enable the determination of the cavity shape from the spectrum analytically.

For the mode localized near the surface of the fiber, $p (=1) \ll m$ and $\mu_{mp} \approx m$. The light will also be confined along the z -axis, if the component of the wave vector along the z -axis, k_z , has two zeros. Quantization rule Eq. (24) is identical to the quantum-mechanical WKB quantization rule with energy $E_{mpq} = k_{mpq}^2 - (m^2/R_0^2)$ and potential $U(z) = [m^2/R(z)^2] - (m^2/R_0^2)$. We arrive at the well-known result that the energy levels E_{mpq} are equally spaced in q with constant $dE_{mpq}/dq = 2k_{mpq} \cdot dk_{mpq}/dq \equiv \Delta E$ for the quadratic potential $U(z)$. The latter corresponds to the fiber shape:

$$R(z) = R_0 [1 + (\Delta k \cdot z)^2]^{-1/2},$$

$$dk_{mpq}/dq = \Delta k = \Delta E \cdot R_0 / 2m,$$

and eigenvalues

$$k_{mpq} = \left[\frac{m^2}{R_0^2} + (q + 1/2) \Delta E m \right]^{1/2}. \quad (25)$$

Here, Δk denotes the curvature of the resonator profile.

The frequency spacing between modes with consecutive quantum numbers q (m) is called the axial (azimuthal) free spectral range and denoted as Δv_q (Δv_m), which can be derived from the eigenvalues k_{mp} of the wave equation ($\nabla^2 + k^2) \cdot E = 0$

$$\Delta v_m = v_{m+1,q} - v_{m,q} = c(k_{m+1,q} - k_{m,q}) \approx c/2\pi n R_0 \quad (26)$$

$$\Delta v_q = v_{m,q+1} - v_{m,q} \approx c \Delta k / 2\pi n. \quad (27)$$

The azimuthal free spectral range (Δv_m) is fixed by the resonator radius. However, the axial mode spacing (Δv_q) depends on the curvature of the resonator profile. Figure 11b indicates the experimentally validated mode structure by visualizing the fluorescence from a resonator doped with erbium ions. Therefore, Δv_q is much smaller than Δv_m without significantly affecting the mode volume of the resonator. With regard to a bottle microresonator with radius $R_0 = 17.5 \mu\text{m}$ and curvature $\Delta k = 0.012 \mu\text{m}^{-1}$, the above formula yields $\Delta v_q = 395 \text{ GHz}$ and $\Delta v_m = 1.9 \text{ THz}$. It is therefore possible to couple light of any arbitrary frequencies to the bottle microresonator by tuning the bottle resonance over one azimuthal free spectral range (from m to $m+1$). Tuning of the resonance frequency over the spectral spacing between adjacent axial modes enables resonant insertion of light at any arbitrary frequencies. The Q-factor

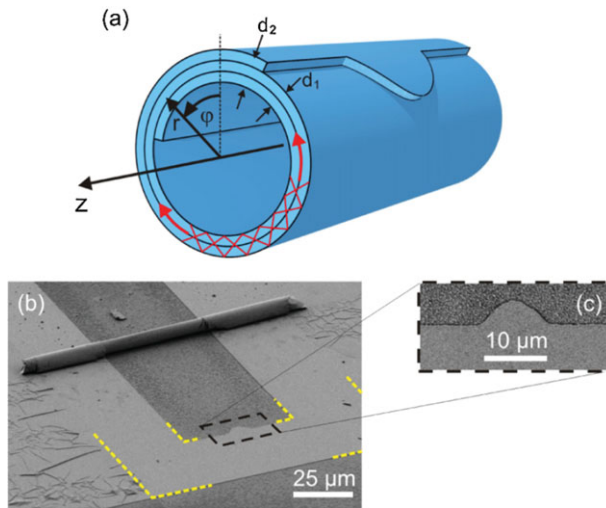


Figure 12 (a) Sketch of a microtube bottle resonator exhibiting a parabolic lobe on its outside rolling edge. Red arrows illustrate the circular light propagation by multiple total internal reflections. (b) SEM image of a microtube bottle resonator. Yellow lines clarify the edges of the U-shaped mesa. (c) Magnified top view on the region marked in (b) [48].

of this type of microresonator should be large enough to avoid radiative loss. The Q-factor of a resonator can be determined by measuring the photon lifetime τ and using the equation $Q = \omega\tau$, where $\omega = 2\pi\nu$ is the angular optical frequency. The Q-factor of bottle WGM microcavities is larger than 10^8 .

3.4.2. Bottle-like self-rolled microtube resonators

The self-rolled-up process has intrinsic advantages in the fabrication of 3D structures by well-established two-dimensional lithography on epitaxially grown samples (Section 4). The radius and wall thickness of rolled-up microtubes are adjusted by the thickness and composition of the bilayers during growth and the winding number can be set by lithography. By adjusting these parameters in the microtube ring resonators, their mode energies can be precisely tuned by the winding number. Microtube resonators have unique properties, for example, very thin layers with an epitaxially smooth surface.

Microtube resonators with a bottle-like geometry can be produced by self-rolling from nanomembranes with a structured rolling edge. Kipp et al. proposed and demonstrated a microtube resonator by rolling up a strained semiconductor bilayer with a parabolic lobe, as shown in Fig. 12 [47]. This parabolic lobe turns the structure into a bottle-like resonator. Two interesting observations are made from the PL spectra in Fig. 13. First, the spatially integrated spectrum shows groups of sharp peaks. In each group, a primary peak is superposed with a group of secondary peaks with equal mode spacing in energy. Secondly, according to the spatially resolved measurement, the modes within a group are localized in special regions along the tube axis. This spatial mode distribution demonstrates that the modes are confined to the lobe position and form a system of higher axial modes.

The physical understanding of the axial modes can be described by the simple model using the adiabatic separation of the azimuthal and axial propagation of light in the microtube, as discussed in Section 2.5. On account of the axial modulation arising from the parabolic lobe of the microtube, a parabolic axial quasipotential, namely $V_{\text{eff}} = az^2 + b$, appears, where a and b are coefficients and z is the axial distance from the center of the microtube. This parabolic potential can lead to groups of axial modes with equidistant frequencies and confinement of mode distribution along the axis. The results from the analytical model, which is further confirmed by the FDTD simulation, agree well with experimental data [47, 102].

The beauty of the microtube bottle resonators is that different field patterns and mode dispersions for a desired application can be precisely tailored. For example, Figs. 13a and b show PL spectra acquired from microtube resonators with a triangular and square lobe. Unlike the parabolic lobe, the axial mode spacing decreases with higher energies in the triangular lobe and increases in the rectangular one. Thus, it is possible to tailor the mode dispersion of the axial modes accurately simply by predefined modulation of the rolling edge [47].

Recently, Mei and coworkers showed that a bottle-like resonator could be produced by rolled-up circular oxide nanomembranes, as shown in Fig. 13c [102]. The PL spectra obtained at room temperature in Fig. 13 show groups of axial modes. These axial modes originate from axial modulation due to the uneven thickness distribution along the microtube axis. Using adiabatic separation, a similar

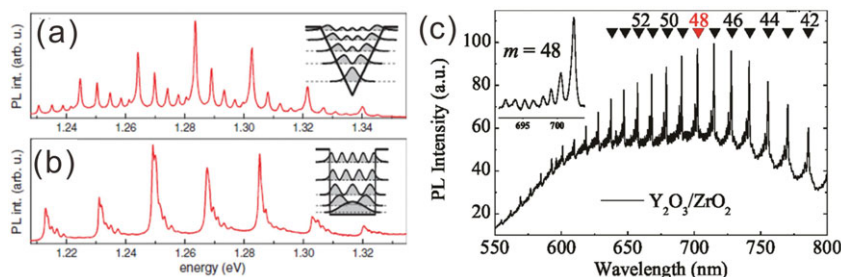


Figure 13 PL spectra of microtube bottle resonators with a (a) triangular and (b) rectangular lobe. The insets sketch the level spacing in a (a) triangular and (b) rectangular potential [48]. (c) The PL spectrum from the middle of a microtubular cavity rolled from a circular $\text{Y}_2\text{O}_3/\text{ZrO}_2$ nanomembrane ($\text{Y}_2\text{O}_3/\text{ZrO}_2$, $n_{\text{eff}} \cong 1.68$). The inset shows the fine structure of a mode with azimuthal number $m = 48$ [102].

axial potential can be obtained leading to the observed axial modes.

4. Design and fabrication of tubular microcavities

Effective fabrication methods of WGM microresonator with a tubular geometry are crucial to optical microdevices in lab-on-a-chip systems. Tubular optical microcavities with good optical properties can be readily produced in the lab from a variety of materials. There are two main techniques: fiber drawing and self-assembly and they will be discussed in this section. Other interesting methods and modification processes will also be touched on briefly.

4.1. Fiber-drawing technique

The traditional and simplest method for the fabrication of optical fiber/tubes is the fiber-drawing technique [126, 133] that is sometimes also referred to as the heat-and-pull technique [134]. In the fiber-drawing technique, the diameter and wall thickness are reduced by heating and pulling the capillaries. The typical process includes two steps: (1) pre-form preparation and (2) fiber drawing.

The process can be used to fabricate thin silica capillaries with a submicrometric wall. In the first step, the intermediate capillaries 150 μm in diameter with a 15- μm thick wall are prepared from a commercial silica tube using a fiber-drawing tower. In the second step, the diameter of the intermediate capillaries is reduced further using a fiber taper rig. Using this technique, glass capillaries with submicrometer wall and diameters several tens of micrometers can be produced. To achieve the desirable wall thickness, the capillary can be further etched with HF ($\sim 10\%$) [133]. Figure 1c shows the scanning electron microscope (SEM) images of glass capillaries fabricated by the fiber-drawing technique [22]. Dye-doped (rhodamine B) tubular polymer (PMMA) optical fibers with different diameters can also be obtained by this technique at 180 $^{\circ}\text{C}$ [40].

As aforementioned, the tubular microcavities with 3D optical confinement have better optical performance. Several improved techniques have been used to fabricate WGMs tubular microresonators with the 3D optical confinement effect and the most important one is the fabrication of bottle microresonators.

The fabrication process for bottle microresonators consists of two steps [52, 134]. Figure 14 shows the schematic of the fiber-pulling rig used to prepare ultrathin optical fibers and bottle microresonators. A uniform hollow fiber can be obtained by the basic fiber-drawing technique described above. It can be accomplished using a hydrogen/oxygen flame or a focused CO_2 -laser beam [14, 52, 134, 135]. These hollow fibers are a few millimeters long and have a diameter corresponding to the desired resonator. In the second step, a bulge between two microtapers is formed on the

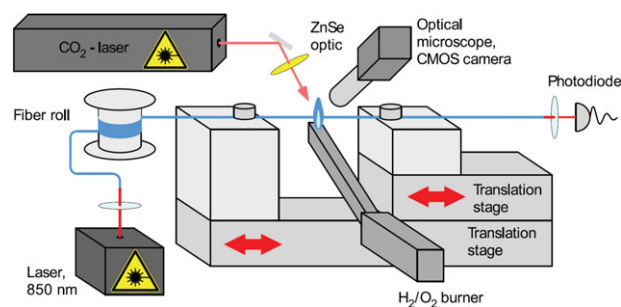


Figure 14 Schematic of the fiber pulling rig used to fabricate ultrathin optical fibers and bottle microresonators. A commercial optical fiber is clamped to two translation stages. One stage is mounted on top of the other. The fiber is then heated by a hydrogen/oxygen flame with a width of 1 mm. The upper stage, called the “stretcher”, elongates the heated fiber, while the lower “translator” moves it relative to the flame (this method is commonly known as the “fiber-drawing technique”). Alternatively, a focused CO_2 -laser beam with a maximum power of 30 W (Synrad, Series 48–2) can be used as a heat source. The laser beam is focused by a ZnSe lens and only heats a 100–150 μm wide section of the fiber. A microscope attached to a CMOS camera captures micrographs of the processed fibers. Throughout the ultrathin optical fiber-pulling process, the transmission of light from a diode laser emitting at a wavelength of 850 nm is monitored [15].

fiber waist [15]. The microtapers are sequentially produced by locally heating the fiber waist with the focused CO_2 -laser beam while the fiber is stretched slightly. The central zone of the bulge exhibits parabolic variations in the fiber diameter and forms the bottle microresonator. By adjusting the CO_2 -laser beam spot size, microtaper separation, and elongation length, the resonator geometry can be fine tuned to obtain the desirable spectral mode spacing.

Recently, a new family of hybrid optical fibers with the tubular geometry composed of conductors, semiconductors, and insulators has been obtained by the conventional preform-based fiber-drawing methods. The fabrication process is illustrated in Fig. 15. A multimaterial tubular geometry is preformed with larger cross-sectional dimensions and short length. This step is critical to the geometry (solid or hollow) and composition of the final fiber. The preform is thermally drawn into multimaterial ‘composite’ fibers consisting of at least two materials having different optical and electrical properties, while maintaining the geometry, increasing the length, and reducing the cross-sectional dimensions. This fiber-drawing process is usually performed in vacuum at a high temperature (typically 10^{-3} torr and 260 $^{\circ}\text{C}$). The key point here is identification of materials that can be codrawn and are capable of maintaining the preform geometry in the final fiber. Multimaterial multifunctional fibers can be fabricated using this method. Examples include polymers (polyether sulfone (PES), polysulfone (PSu), and polyetherimide (PEI)), metals (Sn, In, Bi and eutectics of Au, Bi and Sn), and glass compositions such as As_2Se_3 , As_2S_3 , $\text{As}_{40}\text{Se}_{50}\text{Te}_{10}\text{Sn}_5$, and $\text{Ge}_{15}\text{As}_{25}\text{Se}_{15}\text{Te}_{45}$ [136].

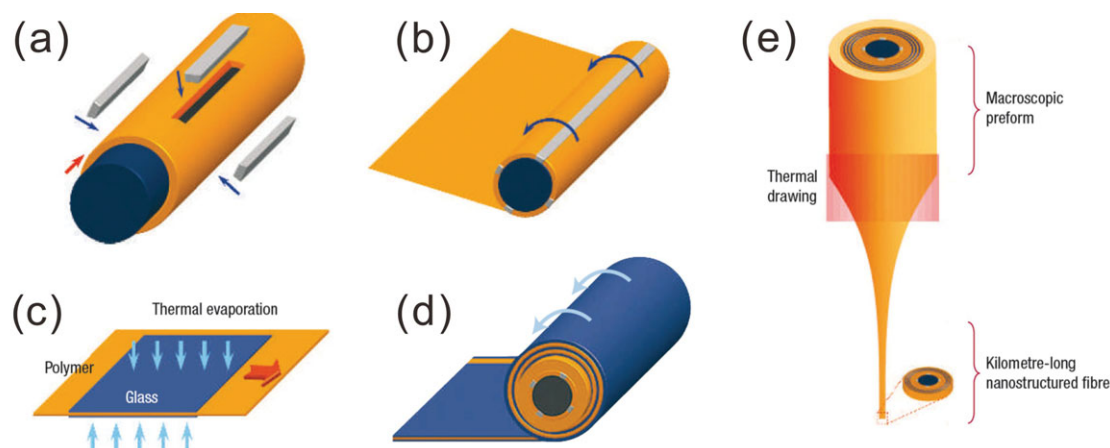


Figure 15 Preform-based fabrication of integrated fiber devices. (a) A chalcogenide semiconducting glass rod is assembled with an insulating polymer shell and four metal electrodes; and (b), a polymer sheet is rolled around the structure to form a protective cladding. (c) The high-index chalcogenide glass is evaporated on both sides of a low-index thin polymer film before (d), being rolled around the cylinder prepared in (a), (b). A polymer layer is wrapped around the coated film for protection. (e) The preform is consolidated in a vacuum oven and is thermally drawn to mesoscopic-scale fibers. The cross section of the resulting fibers retains the same structure and relative sizes of the components at the preform level. Reprinted with permission from refs. [8] and [136].

4.2. Self-rolled-up processes

Nanomembrane wrinkles produced by predefined strain engineering with 3D structures have many potential applications [137]. If the strain gradient is large, the nanomembrane bends into a curved structure and forms a tubular geometry [137]. Since 2000, research on self-rolled-up microtubes fabricated by self-rolling of strained functional layer systems lifted off from a substrate has been prevalent because of potential application in different fields [45, 46, 138]. The micro- and nanotubes obtained by this method have been used in optical resonators [9, 35, 37, 127, 129, 139]. Optical resonances in self-rolled tubular microcavities with subwavelength wall thickness have novel optical properties and researchers have rolled up a variety of materials such as metals, semiconductors, insulators, and polymers [9, 35, 37, 85, 127, 129, 139, 140].

The lift-off technique can be utilized to obtain self-rolled-up tubular microcavities. This method relies on the release of strained thin layers from the substrate by selective etching, as schematically illustrated in Fig. 16. There are two typical procedures for nanomembranes self-rolling. When semiconductor films are deposited by molecular beam epitaxy (MBE), the nanomembrane shaping step follows nanomembrane deposition (Fig. 16a) [45, 141]. However, for metal and oxide thin films, glancing-angle nanomembrane deposition follows sacrificial layer shaping (Fig. 16b) [34, 36, 102]. The typical self-rolled microtubes procedures are described in the following. An etchant-sensitive film is formed on the substrate as a sacrificial layer on which the strained layer is deposited. When the strained layer is freed from the sacrificial layer by selective etching, its top layer contracts and the bottom layer expands. The intrinsic stress gradient causes the bilayer to self-assemble into a tubular microtube. The diameter of microtubes is

tunable by varying the deposition rate, temperature, atmosphere, and layer thickness.

Based on the chemical properties of the strained layer, different materials such as polymers, oxides, and semiconductors are selected as the sacrificial layer. Different thin film deposition processes can be used to obtain the strained layers. A crystalline semiconductor thin film is usually deposited by MBE, metal and insulator thin films are deposited onto the substrate by electron-beam evaporation, and polymer thin films are obtained by spin coating.

The self-rolled-up process can produce tubular microcavities by well-established two-dimensional lithography on epitaxially grown samples. The radius and wall thickness can be adjusted by the thickness and composition of the bilayers and the winding number can be set by lithography. The winding number is determined by the rolling distance divided by the circumference of self-rolled tubes. By adjusting these parameters in the microtube ring resonators, the mode energies can be precisely tuned based on the winding number. The ultrathin wall thickness and tunable optical properties bode well for lab-in-a-tube systems.

4.3. Sundry methods

In order to enhance the Q-factor and widen the applications, other methods can be used to produce tubular optical microcavities.

(1) Rotating deposition on fiber

Rotating deposition proposed by Maqbool et al. produced aluminum nitride WGM microlasers in 2010 [142]. Rare-earth (RE) ions or Ti-doped AlN films are grown using radio-frequency (RF) sputtering in pure nitrogen. The

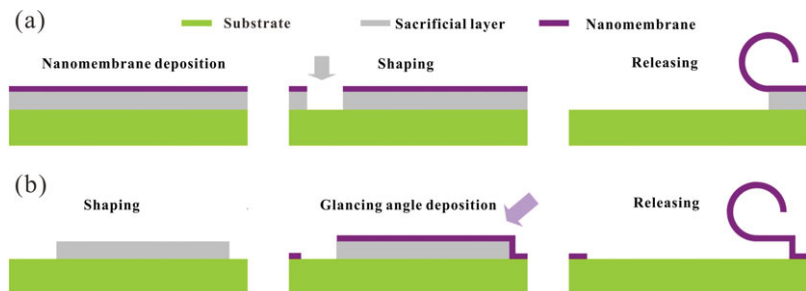


Figure 16 Illustrations of the formation of self-rolled-up microtube: (a) inorganic self-rolled-up procedure; (b) organic-based self-rolled-up procedure.

thickness and composition of the inorganic films around the optical fibers is controllable. The optical fibers are clamped to the rotating metallic substrate holder and during film deposition, the substrate is rotated constantly to realize uniform deposition around the fiber (see the schematic in Fig. 17a) [142]. This process is quite effective in producing high-index inorganic crystalline tubular WGM microcavities [142].

(2) Template method

Optical microcavities can be prepared using templates such as the microchannel glass matrix [54] and porous anodic alumina membranes [143]. The typical procedures are illustrated in Fig. 17b and described below. (a) Choice of templates: The diameter of the final microcavities is influenced by the diameter of the channel in the template. The anodic alumina membrane with uniform pore diameter is adjustable from 20 to 200 nm [143] and the diameter of channels in the microchannel glass matrix is around several micrometers [54]. (b) Filling the microchannels in the template by the flexible precursor materials: The suitable precursor materials are used to fill the channels of the template. Different solutions, sol, monomer or fusions at high temperature are suitable as precursor materials. (c) Solidification. (d) Removal of the templates. After solidification of the precursor materials, individual micro-/nanocylinder microcavities are obtained after removing the templates.

Different kinds of materials including inorganic materials and polymer cylinders can be obtained by this method. For instance, Rakovich et al. prepared microtube cavities with Q-factors up to 3200 using simple vacuum-assisted wetting and filtration through a microchannel glass matrix [54]. O'Carroll et al. observed the microcavities effects and optically pumped the laser in polymer nanowires fabricated with an anodic alumina membrane template [143].

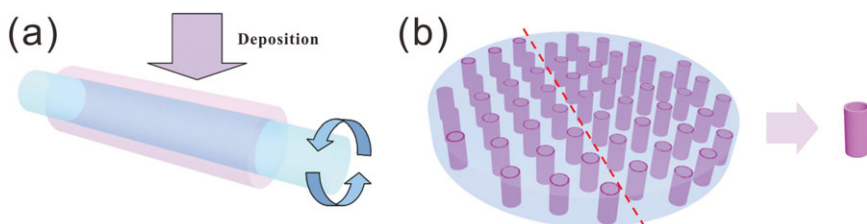


Figure 17 (a) Scheme for the rotating deposition of AlN tubular microlaser [142]. (b) The formation procedures of individual microtubes from the template method [54, 143].

(3) Electrospinning

Among the fabrication methods to generate one-dimensional (1D) nanostructures, electrospinning is a straightforward, cost-effective, and versatile method to produce nanofibers from a variety of materials such as polymers, inorganic materials, and hybrid compounds [144]. Other complex structures including core/shell fibers can be obtained by multifluidic coaxial electrospinning. 3D microcavities have been fabricated by relatively simple and controllable electrospinning soft methods [55]. The approach is based on electrospinning of dye-doped polymer fibers utilizing this versatile technique to spin fibers of various dimensions and geometries including coaxial structures [55].

Besides the aforementioned fabrication methods, photolithographic and etching procedures are used to prepare tubular microcavities [145, 146]. With the development of micro-/nanotechnology, new methods will be introduced. The ability to combine novel physical and chemical functions (such as quantum dots [141, 147] or upconversion luminescence [15]) using the proper methods creates enormous opportunities for scientific discovery and research of optical devices.

5. Applications of tubular optical microcavities

Excellent fabrication processes and rigorous theoretical simulation have rendered tubular microcavities useful in a wide range of applications that take advantage of the unique optical properties such as refractive index, fluorescence, Raman scattering, and optical absorption. Theoretically, the application of tubular optical microcavities is related to the evanescent wave and geometry. The cylindrical channel nature of tubular optical microcavities and unique properties of fluids can be utilized to design and

fabricate novel devices with superior performance. The fluids can be used as carriers of nanoparticles (quantum dots), cells, and molecular species. In this section, some of the important applications of WGM tubular microcavities are discussed. Examples include opto-/microfluidics, microlasers, and bio-/chemsensing.

5.1. Optomicrofluidics

Since its emergence, optofluidics offers a robust platform for excellent enabling simultaneous delivery of optics and fluids with microscopic precision. Fluids have unique properties that cannot be found in solid equivalents, and these properties can be used to design novel devices that have the ability to change the optical properties of the fluid medium in the device by simply replacing the fluid. Other characteristics include the optically smooth interface between two immiscible fluids, the ability of flowing streams of miscible fluids to create gradients in optical properties by diffusion, and the ability of carrying nanoparticles (quantum dots), cells, and molecules [148]. Tubular optical microresonators possess natural channels for fluid flow and hence, they are suitable for optomicrofluidic devices and integrated systems. Microfluidics offers a number of advantages, for example, use of extremely small amounts of reagents and samples, ultrahigh sensitivity; high throughput, possible sample processing before detection, short analysis time, in situ monitoring, and low cost [120]. The large surface area-to-volume ratio and mass transport by nondiffusive means offers the potential for transduction of analytes in seconds to minutes. Termed “marriage of optics and fluidics” and “combination of integrated optical and fluidic components in the same miniaturized system”, optomicrofluidics can operate on the system level, for example, lab-on-a-chip or micrototal analysis [56]. In optomicrofluidic devices, the phenomenon is related to total internal reflection and evanescent waves play important roles in device fabrication based on tubular optical microcavities [148]. The first microfluidic device was a miniaturized gas chromatography (GC) system reported by Terry et al. at Stanford University in the 1970s [149]. Moon et al. and Fan et al. investigated optomicrofluidics in tubular structures and the main application is the microfluidic laser [82, 87, 133, 150]. In order to enhance the sensitivity, new structures have been suggested. For example, ultrahigh sensitivity has been achieved from an active sensor structure coupled to an optofluidic ring laser producing a sensitivity of 5930 nm/RIU [51]. This ultrahigh sensitivity is two orders of magnitude higher than that of a conventional ring-resonator sensor [51].

The fluid properties can be exploited to produce highly flexible, tunable, and reconfigurable photonic microdevices. The self-rolled nanotechnology not only enables the fabrication of optomicrofluidic devices, but also shows great potential in self-rolled microfluidic devices. In 2006, It is reported that 3D InGaAs/GaAs self-rolled microtubes can be integrated on substrate as fluidic channels [151]. The results indicate the possibility of using self-rolled microtubular cavities in microfluidics. In 2007, Luchnikov

et al. reported self-rolled polymer microtubes in microfluidics systems [140] and later, Harzim et al. demonstrated that an optofluidic tubular resonator with a large Q-factor (2900) and high sensitivity of up to 880 nm/RIU could be fabricated by the self-rolled-up process based on SiO₂ [127]. These are milestone studies promoting the development label-free on-chip integration of inorganic self-rolled-up optical microcavities in lab-in-a-tube optomicrofluidic devices.

5.2. Microlasers

The acronym LASER is derived from the phrase “light amplification by stimulated emission of radiation” [152]. The light emission is characteristic of and influenced by the specific gain medium and resonator [152, 153]. As a basic building block, micro- or nanolasers with small size and low power can be integrated on a chip to enable high speed operation [1, 154]. Microcavities provide excellent coupling of spontaneous emission into lasing modes and a high Q-factor that consequently leads to low lasing threshold. The tubular optical microcavities with (ultra-)high Q-factors are suitable for (ultra-)low threshold microlasers.

Organic semiconductors, dye-doped polymers [155], dye-doped liquids, quantum dots, and rare-earth-doped inorganic materials are now popular optical gain dopants in the field of tubular microlasers. The first demonstration of dye-doped polymer WGMs microresonators with a tubular geometry undergoing lasing action was reported over fifty years ago [114, 115, 156]. Interest in the study and application of tubular WGMs microcavities as low threshold microlasers has proliferated since then. The first organic semiconductor microlasers reported had a threshold of 300 $\mu\text{J}/\text{cm}^2$ by Tessler et al. [28] and Frolov et al. discussed the photo-pumped multimode and single mode lasing formed by thin films of luminescent organic semiconductor with a Q-factor of around 5000 [117, 118, 157]. Very low threshold pulse energies of 100 pJ have been reported in these organic semiconductor microlaser [118] and Ti-doped AlN WGM microlasers on optical fibers with a Q-factor higher than 1500 were deposited using RF sputter-deposition [142]. A threshold power of 24 mW was observed from this AlN microlaser [142] and Er-doped upconversion luminescent glass capillaries were used to fabricate bottle-like tubular microlasers with 3D optical confinement [14, 135]. Malko demonstrated the regime of microtubular lasing and WGMs using CdSe nanocrystal quantum dots solids incorporated into microcapillary tubes in 2002 [158]. Lasing in self-rolled semiconductor microtubes was reported at room temperature. Self-organized InGaAs/GaAs quantum dots were incorporated as the gain medium and the microlaser had an ultralow threshold ($\sim 4 \mu\text{W}$) and minimum intrinsic linewidth of $\sim 0.2\text{--}0.3 \text{ nm}$ at room temperature. The maximum intrinsic Q-factor measured under low pump power was ~ 3500 [58]. The typical liquid dye-doped laser used a solution of organic dye molecules in a solvent such as the optical gain medium [83, 86, 87]. Lasing was achieved by

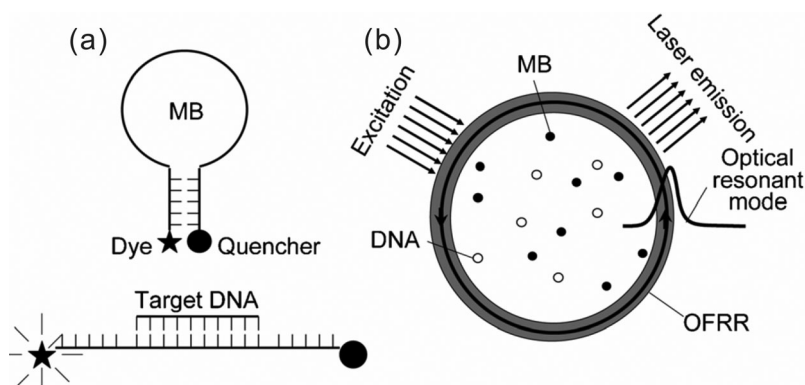


Figure 18 (a) The molecular beacon (MB) fluorescence is quenched when it is in the closed state. MB fluorescence is restored upon hybridization with the target DNA. (b) Intracavity DNA detection and differentiation with the optofluidic ring resonator (OFRR) laser [50].

surrounding a small section of the glass capillary with a solution of Rh 6G and by coupling the pumping light into the capillary wall. The Q-factor is higher than 10^4 and the lasing threshold pump energy was ~ 100 nJ/pulse at a pulse duration of 6 ns [86]. The Q-factors of this type of microcavities are always quite high ($>10^4$). Moon et al. and other groups improved this type of microlaser and found several unique features. Compared to dye-doped liquid core microlasers in which an optical hollow/solid fiber was inserted into the same glass capillary, WGM laser oscillation was achieved at a low-threshold pump energy of ~ 200 μ J [87, 150]. Subsequently, this structure was used to demonstrate laser oscillation with colloidal semiconductor CdSe/ZnS quantum rods as the lasing gain medium [122, 159].

Attempts are being made to produce tunable and flexible microlasers. The luminescent characteristics of Förster or fluorescence resonance energy transfer (FRET) are used as the gain medium. Fan and coworkers fabricated optofluidic FRET lasers using DNA scaffolds (Fig. 18) [50, 160, 161]. The rate of energy transfer depends on many factors such as the extent of spectral overlap, relative orientation of the transition dipoles, and most importantly, distance between the donor and acceptor molecules [162]. As a result, efficient FRET lasing is achieved at an unusually low acceptor concentration of micromolar and it is over 1000 times lower than that in conventional optofluidic dye lasers. The lasing threshold is of the order of μ J/mm². Various DNA-scaffold FRET lasers are demonstrated to illustrate large possibilities in optofluidic laser designs. The work is paving the way for many applications such as lab-in-a-tube bio/chemsensing, biocontrolled photonic devices, and biophysics [50, 160].

A new type of fiber laser proposed by Shapira and coworkers has found a plethora of unique functions in both fundamental science and applications [163–165]. Low-threshold (86 nJ) lasers at nine different wavelengths were demonstrated throughout the visible and near-infrared regions with an organic laser dye incorporated into a copolymer matrix core [163]. This has led to an important development in the field: radially isotropic lasing using a hollow-core Bragg fiber in combination with organic dye-doped water-solution plugs placed inside the fiber core acting as azimuthally isotropic gain media [164]. This setup

allows new designs to produce highly coherent ring-like radiation with inherent wavelength scalability and control over the position, direction, and polarization of the lasing wavefront [165]. The most important advantage of the liquid dye-doped core microlaser is the ability to integrate with other optical and microfluidic functions to build complete “lab-on-a-chip” or “lab-in-a-tube” microsystems and these new types of microlasers constitute microlight source that have many applications.

5.3. Bio-/chemsensing

Optical bio-/chemsensors are powerful detection and analysis tools in biomedical research, healthcare, pharmaceuticals, and environmental monitoring. The typical optical properties including refractive index [4, 87, 126], fluorescence [50, 160, 166], and optical absorption [167], have been used in microtubular optical resonators to generate sensing signals. The tubular geometry is suitable for liquids used as carriers of analytes and the evanescent wave is important to the fabrication of bio-/chemsensing devices [111]. Therefore, tubular optical microcavities can be used as effective sensors for liquids [9, 35, 37], single molecules [168], DNA [50, 57, 113, 160], proteins [169], virus, bacteria, cells [49], and nanoparticles (Fig. 19) [13, 170, 171]. Generally, fluorescence-based detection and label-free detection are the two main protocols implemented in optical biosensing using a tubular geometry.

Refractive-index changes within the capillary core are probed by the evanescent field that interacts with molecules near the inner wall [172]. The interaction between the analytes and evanescent wave increases the path length and wavelengths of light through the resonance. The effective refractive-index change leads to an azimuthal mode shift in the spectra that can be used to detect analytes [111, 170].

The sensitivity of the optofluidic ring resonator (OFRR) is measured in units of nm per refractive-index unit (nm/RIU). Different types of microresonators show different sensitivities. The typical approach uses a quartz capillary as the fluidics and ring resonator to form the liquid-core optical ring resonator. The sensitivity is 16.1 nm/RIU and the detection limit of this system is around 5×10^{-6} RIU [4]. The optofluidic ring resonator (OFRR) is able

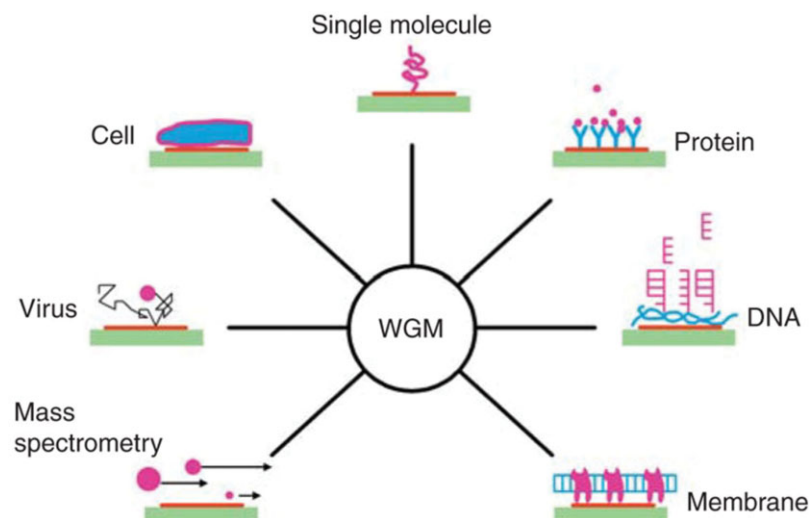


Figure 19 Applications of WGM biosensors for analysis of various biological materials in different configurations [13].

to detect HER2 at medically relevant concentrations in serum ranging from 13 to 100 ng/mL in 30 min [169]. Owing to the large Q-factor, OFRR can achieve a refractive-index detection limit of 10^{-7} RIU and mass detection limit of sub-pg/mm², on a par with the most sensitive biosensors. The OFRR has been applied to many biomedical applications including CD4+ and CD8+ T-lymphocyte detection [49], viral particle detection [173], and DNA detection [50, 57, 113]. The label-free, rapid, and sensitive optical sensor used in whole-cell detection of CD4+ and CD8+ T-Lymphocytes, and CD4+ cell lysis detection results show distinguishable detection ranges around and below 200 CD4+ cells per μ L and up to 320 CD4+ cells per μ L [173]. Bulk DNA detection of 10 pM 25-mer has been achieved and the actual limit of detection is significantly lower. The mass loading limit of detection is estimated to be 4 pg/mm² [57, 113]. Recently, rapid detection of the cancer biomarker CA15–3 using serological samples from breast cancer patients was achieved [174]. The device consisted of a microcapillary in a sensitivity of 570 nm/RIU having a layer of fluorescent silicon quantum dots (QDs) coated on the channel surface and a Q-factor of 1.2×10^5 was demonstrated [175]. In small-molecule detection, 10 nM biotin was detected with a surface mass density of 1.6 pg/mm² and the detection limit was approximately 0.14 pg/mm² [175].

Self-rolled microtubes with (ultra-)thin walls exhibit higher sensitivity than glass capillaries and have been used in lab-in-a-tube sensors [176]. With the development of fabrication technology, SiO/SiO₂ bilayer self-rolled-up optical microcavities were used as real-time lab-on-a-chip sensor [9], and a sensitivity of up to 880 nm/RIU and the minimum detection limit of 3.4×10^{-4} RIU [37] was achieved from this kind of optical resonators. Immobilization of DNA and fluorescent proteins in nanostructured fibers can be used, among others, for in vivo gene expression and biosensing applications of the polymer self-rolled microtubes [177]. Various self-rolled microtube structure fabricated from biocompatible materials have been applied to cell-culture analysis, including mouse cells [178], yeast cells [36], neuron

cells [139] and HeLa cells [127, 129]. As a suitable alternative to inorganic materials, organic polymers exhibit better biocompatibility and can mimic the in vivo microenvironment. They have been used to study the in situ seeding of yeast cells [140]. A strategy has been proposed to fabricate tubular structures with layered walls made of multiple types of orientated cells in rolled-up organic tubular structures. This circumvents the principal structural limitations of tubular tissue biomimicry [179] and this method may be widely used in simulation of tubular tissues [179].

5.4. Mechanical sensing and thermometry

High Q-factor WGMs microresonators with a tubular geometry increase the mechanical and temperature sensitivity. The mechanical tunability in two spherical resonators coupled to the evanescent field was analyzed theoretically and tested experimentally in 1994 [180]. WGMs resonators possess the morphology-dependent resonance features. The positions of the WGMs resonances are strain sensitive and can be tuned in a controlled manner by applying strain with a piezoelectric transducer. The measured wavelength shifts yield a linear slope of 0.14 nm/mstrain, in good agreement with calculated shifts based on published data for the elastic moduli and the strain-optic coefficients for fused quartz [181]. This process can be used in other tubular resonators to prepare mechanical sensors. The emission spectra of microring lasers fabricated from π -conjugated polymer films cast on nylon microfibers with diameters in the range of 35–90 μ m were studied by applying uniaxial stress with strain of up to $\sim 12\%$. The laser emission spectra change substantially with the applied stress, showing enhanced sensitivity to stress over changes induced in the fiber diameter alone [182]. The ultrahigh Q-factor (3.6×10^8) WGMs “bottle microresonators” with 3D optical confinement can be fabricated from standard optical glass fibers. The maximum stress applied to this kind “bottle microresonators” is limited by the travel range of the bending actuator. It can be inferred from the frequency shift to be about 35% of the

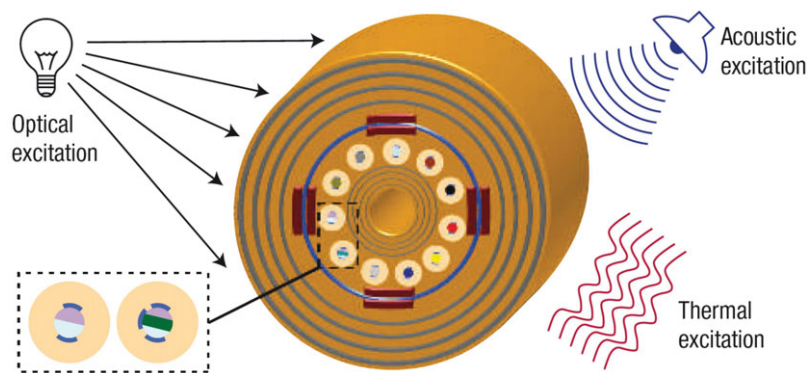


Figure 20 Future vision of integrated lab-in-a-tube system. A single tube consists of thin-film semiconducting devices, and also multiple devices distributed over the cross section, with each device sensitive to a different environmental parameter (light, heat, acoustic waves, mechanical force and so on) [136].

typical damage threshold of the silica resonator structure [14].

An active, tunable optical fiber can incorporate multiple microfluidic channels into interior fiber microchannels, and present temperature-dependent tunability of ~ 0.10 nm/°C or ~ 0.014 nm/mW of power to the grating microheater [183]. Suter et al. presented a thorough temperature-dependence calibration technique for the liquid-core optical ring resonator [16] and their results indicated that the liquid-core optical ring resonator could be used in thermometry.

5.5. Other applications

Tubular optical microresonators are used in micro-lasers, optomicrofluidics, and bio-/chemsensors [184]. A metamaterials-based hyperlens offers the possibility to break the limitation of the diffraction limit of light. It was proposed that a magnifying superlens could be constructed by using cylindrical metamaterials [185]. The rolled-up nanotechnology is the perfect approach to create these multilayered stacked structures while at the same time reducing the number of processing steps required. By simply rolling up multilayered metals and oxides (or semiconductors), multilayer stacked metamaterials can be created with a tubular geometry and these multilayered stacked metamaterials are useful in hyperlens devices for imaging [70, 176, 186–188].

6. Summary and Outlook

This review summarizes recent progress in the field of optical microresonators with a tubular geometry that boast a large Q-factor and high sensitivity in terms of fundamental properties, fabrication protocols, 3D light confinement design, and applications. Although much research has been conducted, turning these principle designs into practical applications still requires more work. Inspired by the applications and research methods of other WGMs optical microcavities such as microspheres, microdisks, and toroids, new and exciting ideas and designs pertaining to WGMs optical microcavities with the tubular geometry is gaining

much attention in the three areas of new materials, higher quality, and functional integration.

New materials are needed for next-generation microdevices and investigating isolated components in a device or system is no longer sufficient to solve technological problems associated with the development of an environmentally benign energy infrastructure [189]. Different inorganic and organic materials with special functions are suitable alternatives and upconversion luminescent materials, electroluminescent materials, piezoelectric materials, and semiconductors can be used to fabricate tubular optical microtubes. These novel materials can introduce special electronic, electromechanical, thermoelectric, optoelectronic, optomechanical and photonic properties leading to better and smarter devices. Smart materials such as metal-insulator phase-transition materials and environmentally sensitive PVA-PAA hydrogel [190], will introduce new functions to optical microtubes and tunable optical microresonators comprising smart materials can be used to fabricate next-generation optical components and optical bio-/chemsensing devices.

As one basic parameter, the Q-factor is crucial to applications of optical microcavities. So far, optical microcavities with (ultra-)large Q-factors have more applications than ones with smaller Q-factor counterparts. However, the structures in WGM resonators with a small Q-factor facilitates coupling of light to the resonant modes leading to substantial enhancement in the light path in the active materials and subsequently improved absorption [191]. Cavity-enhanced radiation-pressure coupling of the optical and mechanical degrees of freedom gives rise to a range of optomechanical phenomena, particularly providing a route to the quantum regime of mesoscopic mechanical oscillators [192]. Micro- and nano-optomechanics has recently attracted great interest because of applications ranging from mechanical sensing to signal processing as well as fundamental research of mesoscale quantum mechanics [193, 194].

Future development of tubular optical microresonators lies in many aspects including fundamental science, engineering, and applications. Future research will produce more sophisticated functionalities such as truly multifunctional fabrics. The evanescent-wave effect should not be ignored in future research and better understanding of the evanescent wave and interactions with materials with

special functions will lead to better tubular optical microcavities in complex systems with integrated functions. One typical example is the multimaterials multifunctional fiber that can see, hear, sense, and communicate (Fig. 20) [191] and lab-in-a-tube microsystem [38]. Continuous efforts are expected to bring creative ideas to enable wider applications of microcavities and better micro- and nanosystems.

Acknowledgements. This work is supported by the Natural Science Foundation of China (Nos. 61008029 and 51102049), the Program for New Century Excellent Talents in University (No. NCE10-0345), the Shanghai Pujiang Program (No.11PJ1400900), the Specialized Research Fund for the Doctoral Program of Higher Education of China (No. 20110071120009), the China Postdoctoral Science Foundation Funded Project (No. 2011M500731), the Hong Kong Research Grants Council (RGC) General Research Funds (GRF) Nos. 112510 and 112212, and the City University of Hong Kong Applied Research Grant (ARG) 9667066.

Received: 15 March 2013, **Revised:** 3 June 2013,

Accepted: 5 June 2013

Published online: 1 July 2013

Key words: Tubular geometry, WGM, microcavity, resonator, tube, sensor.



Jiao Wang completed her BS degrees in Materials Chemistry at Lanzhou University, China (2006). She received her PhD Degree in Materials Chemistry and Physics on rare-earth luminescent materials from the Key Laboratory of Transparent Optofunctional Inorganic Materials of Chinese Academy of Sciences, Shanghai Institute of Ceramics, Chinese Academy of Sciences, China (2011). She

currently holds a postdoctoral fellowship in the Department of Materials Science in Fudan University, China. Her current research interest focuses on optical properties and applications of optical microcavities and metamaterials.



Tianrong Zhan received the Ph.D. degree in Physics from Fudan University, China, in 2012, where he conducted research in the field of photonic crystals and plasmonics. He went onto research tubular optical microcavities at Fudan University as a research assistant. He is a Post-doctoral Scholar at the University of Delaware since 2013. His current research

interests include metamaterials and graphene plasmonics.

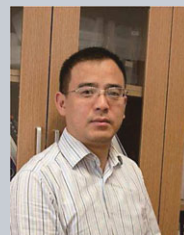


Gaoshan Huang received his Ph.D. in condensed-matter physics at the Nanjing University, China in 2007. After graduation, he worked in IFW Dresden, Germany as a guest scientist for two years. Then he moved to IMRE, Singapore as a research engineer. In 2010, he joined the Department of Materials Science, Fudan University, China, as an associate profes-

sor. His current research interest is the fabrication and characterization of low-dimensional structures.



Paul K Chu received his PhD in chemistry from Cornell University and is presently Chair Professor of Materials Engineering in the City University of Hong Kong. His research activities encompass plasma surface engineering and materials science. He is Chairman of the Plasma-Based Ion Implantation (PBII&D) International Committee, a member of the Ion Implantation Technology (IIT) International Committee and IEEE Nuclear and Plasma Science Society Fellow Evaluation Committee, senior editor of IEEE Transactions on Plasma Science, and associate editor of Materials Science & Engineering Reports. He is a Fellow of the APS, AVS, IEEE, and MRS.



Yongfeng Mei received his BS and MS in physics from Nanjing University and PhD in physics and materials science from City University of Hong Kong. He is a full professor in materials chemistry and physics in the Department of Materials Science in Fudan University. Before that, he worked as a post-doctoral researcher in the Max Planck Institute for Solid State Research and then led a research group

in the Leibniz Institute for Solid State and Materials Research, Dresden. His research interest focuses on the development of novel inorganic nanomembranes and their properties in optics, optoelectronics and micro-/nanoscale mechanics.

References

- [1] M. Smit, J. van der Tol, and M. Hill, *Laser Photon. Rev.* **6**, 1–13 (2012).
- [2] V. S. Ilchenko and A. B. Matsko, *IEEE J. Sel. Top. Quantum Electron.* **12**, 15–32 (2006).
- [3] A. B. Matsko and V. S. Ilchenko, *IEEE J. Sel. Top. Quantum Electron.* **12**, 3–14 (2006).
- [4] I. M. White, H. Y. Zhu, J. D. Suter, N. M. Hanumegowda, H. Oveys, M. Zourob, and X. D. Fan, *IEEE Sens. J.* **7**, 28–35 (2007).
- [5] Y. Yamamoto and R. E. Slusher, *Phys. Today* **46**, 66–73 (1993).
- [6] K. J. Vahala, *Nature* **424**, 839–846 (2003).
- [7] M. Kuwatagonokami, R. H. Jordan, A. Dodabalapur, H. E. Katz, M. L. Schilling, and R. E. Slusher, *Opt. Lett.* **20**, 2093–2095 (1995).
- [8] M. Bayindir, A. F. Abouraddy, J. Arnold, J. D. Joannopoulos, and Y. Fink, *Adv. Mater.* **18**, 845–849 (2006).
- [9] G. Huang, V. A. Bolanos Quinones, F. Ding, S. Kiravittaya, Y. Mei, and O. G. Schmidt, *ACS Nano* **4**, 3123–3130 (2010).
- [10] J. Hecht, *Opt. Photon. News* **10**, 26–30 (1999).
- [11] L. Rayleigh, *Scientific Papers* **5**, 617–620 (1912).

- [12] A. Chiasera, Y. Dumeige, P. Feron, M. Ferrari, Y. Jestin, G. N. Conti, S. Pelli, S. Soria, and G. C. Righini, *Laser Photon. Rev.* **4**, 457–482 (2010).
- [13] F. Vollmer and S. Arnold, *Nature Methods* **5**, 591–596 (2008).
- [14] M. Poellinger, D. O’Shea, F. Warken, and A. Rauschenbeutel, *Phys. Rev. Lett.* **103**, 053901 (2009).
- [15] D. O’Shea, C. Junge, M. Poellinger, A. Vogler, and A. Rauschenbeutel, *Appl. Phys. B* **105**, 129–148 (2011).
- [16] J. D. Suter, I. M. White, H. Y. Zhu, and X. D. Fan, *Appl. Opt.* **46**, 389–396 (2007).
- [17] C. G. B. Garrett, W. Kaiser, and W. L. Bond, *Phys. Rev.* **124**, 1807–1809 (1961).
- [18] S. X. Qian, J. B. Snow, H. M. Tzeng, and R. K. Chang, *Science* **231**, 486–488 (1986).
- [19] D. K. Armani, T. J. Kippenberg, S. M. Spillane, and K. J. Vahala, *Nature* **421**, 925–928 (2003).
- [20] W. Bogaerts, P. De Heyn, T. Van Vaerenbergh, K. De Vos, S. K. Selvaraja, T. Claes, P. Dumon, P. Bienstman, D. Van Thourhout, and R. Baets, *Laser Photon. Rev.* **6**, 47–73 (2012).
- [21] S. Feng, T. Lei, H. Chen, H. Cai, X. Luo, and A. W. Poon, *Laser Photon. Rev.* **6**, 145–177 (2012).
- [22] V. Zamora, A. Diez, M. V. Andres, and B. Gimeno, *Photonic Nanostruct.* **9**, 149–158 (2011).
- [23] M. Cai, O. Painter, and K. J. Vahala, *Phys. Rev. Lett.* **85**, 74–77 (2000).
- [24] S. Lacey, H. Wang, D. H. Foster, and J. U. Nockel, *Phys. Rev. Lett.* **91**, 4 (2003).
- [25] S. V. Frolov, A. Fujii, D. Chinn, Z. V. Vardeny, K. Yoshino, and R. V. Gregory, *Appl. Phys. Lett.* **72**, 2811–2813 (1998).
- [26] Y. Yoshida, T. Nishimura, A. Fujii, M. Ozaki, and K. Yoshino, *Appl. Phys. Lett.* **86**, 141903 (2005).
- [27] H. Yanagi, R. Takeaki, S. Tomita, A. Ishizumi, F. Sasaki, K. Yamashita, and K. Oe, *Appl. Phys. Lett.* **95**, 033306 (2009).
- [28] N. Tessler, G. J. Denton, and R. H. Friend, *Nature* **382**, 695–697 (1996).
- [29] Z. Li and D. Psaltis, *Microfluid. Nanofluid.* **4**, 145–158 (2008).
- [30] Y. Mei, G. Huang, A. A. Solovov, E. B. Urena, I. Moench, F. Ding, T. Reindl, R. K. Y. Fu, P. K. Chu, and O. G. Schmidt, *Adv. Mater.* **20**, 4085–4090 (2008).
- [31] P. E. Barclay, K.-M. C. Fu, C. Santori, and R. G. Beausoleil, *Appl. Phys. Lett.* **95**, 191115 (2009).
- [32] C. F. Wang, Y. S. Choi, J. C. Lee, E. L. Hu, J. Yang, and J. E. Butler, *Appl. Phys. Lett.* **90**, 081110 (2007).
- [33] J. Ward and O. Benson, *Laser Photon. Rev.* **5**, 553–570 (2011).
- [34] G. S. Huang, S. Kiravittaya, V. A. B. Quinones, F. Ding, M. Benyoucef, A. Rastelli, Y. F. Mei, and O. G. Schmidt, *Appl. Phys. Lett.* **94**, 141901 (2009).
- [35] A. Bernardi, S. Kiravittaya, A. Rastelli, R. Songmuang, D. J. Thurmer, M. Benyoucef, and O. G. Schmidt, *Appl. Phys. Lett.* **93**, 094106 (2008).
- [36] G. S. Huang, Y. F. Mei, D. J. Thurmer, E. Coric, and O. G. Schmidt, *Lab Chip* **9**, 263–268 (2009).
- [37] S. M. Harazim, V. A. Bolanos Quinones, S. Kiravittaya, S. Sanchez, and O. Schmidt, *Lab Chip* **12**, 2649–2655 (2012).
- [38] E. J. Smith, W. Xi, D. Makarov, I. Monch, S. Harazim, V. A. Bolanos Quinones, C. K. Schmidt, Y. Mei, S. Sanchez, and O. G. Schmidt, *Lab Chip* **12**, 1917–1931 (2012).
- [39] H. P. Weber and R. Ulrich, *Appl. Phys. Lett.* **19**, 38–40 (1971).
- [40] M. Kailasnath, V. P. N. Nampoori, and P. Radhakrishnan, *Pramana J. Phys.* **75**, 923–927 (2010).
- [41] J. C. Knight, H. S. T. Driver, and G. N. Robertson, *Opt. Lett.* **18**, 1296–1298 (1993).
- [42] J. C. Knight, H. S. T. Driver, and G. N. Robertson, *J. Opt. Soc. Am. B* **11**, 2046–2053 (1994).
- [43] M. V. Artemyev, U. Woggon, and R. Wannemacher, *Appl. Phys. Lett.* **78**, 1032–1034 (2001).
- [44] P. Bianucci, X. Wang, J. G. C. Veinot, and A. Meldrum, *Opt. Exp.* **18**, 8466–8481 (2010).
- [45] V. Y. Prinz, V. A. Seleznev, A. K. Gutakovskiy, A. V. Chehovskiy, V. V. Preobrazhenskii, M. A. Putyato, and T. A. Gavrilova, *Physica E* **6**, 828–831 (2000).
- [46] O. G. Schmidt and K. Eberl, *Nature* **410**, 168–168 (2001).
- [47] T. Kipp, H. Welsch, C. Strelow, C. Heyn, and D. Heitmann, *Phys. Rev. Lett.* **96**, 077403 (2006).
- [48] C. Strelow, H. Rehberg, C. M. Schultz, H. Welsch, C. Heyn, D. Heitmann, and T. Kipp, *Phys. Rev. Lett.* **101**, 127403 (2008).
- [49] J. T. Gohring and X. D. Fan, *Sensors* **10**, 5798–5808 (2010).
- [50] Y. Sun and X. Fan, *Angew. Chem. Int. Ed.* **51**, 1236–1239 (2012).
- [51] X. Zhang, L. Ren, X. Wu, H. Li, L. Liu, and L. Xu, *Opt. Exp.* **19**, 22242–22247 (2011).
- [52] M. Sumetsky, *Opt. Lett.* **29**, 8–10 (2004).
- [53] M. Poellinger and A. Rauschenbeutel, *Opt. Exp.* **18**, 17764–17775 (2010).
- [54] Y. P. Rakovich, S. Balakrishnan, J. F. Donegan, T. S. Perova, R. A. Moore, and Y. K. Gun’ko, *Adv. Funct. Mater.* **17**, 1106–1114 (2007).
- [55] A. J. Das, C. Lafargue, M. Lebental, J. Zyss, and K. S. Narayan, *Appl. Phys. Lett.* **99**, 263303 (2011).
- [56] H. Schmidt and A. R. Hawkins, *Nature Photon.* **5**, 598–604 (2011).
- [57] J. D. Suter, D. J. Howard, H. D. Shi, C. W. Caldwell, and X. D. Fan, *Biosens. Bioelectron.* **26**, 1016–1020 (2010).
- [58] F. Li and Z. Mi, *Opt. Exp.* **17**, 19933–19939 (2009).
- [59] A. Taflove and S. C. Hagness, *Computational Electrodynamics: The Finite-Difference Time-Domain Method* (Artech, Norwood, MA, 2000).
- [60] K. S. Yee, *IEEE Trans. Antennas Propagat.* **AP-14**, 302–307 (1966).
- [61] J.-P. Berenger, *J. Comput. Phys.* **114**, 185–200 (1994).
- [62] S. D. Gedney, *IEEE Trans. Antennas Propagat.* **44**, 1630–1639 (1996).
- [63] M. Hosoda and T. Shigaki, *Appl. Phys. Lett.* **90**, 181107 (2007).
- [64] P. Bermel, E. Lidorikis, Y. Fink, and J. D. Joannopoulos, *Phys. Rev. B* **73**, 165125 (2006).
- [65] A. Fang, T. Koschny, M. Wegener, and C. M. Soukoulis, *Phys. Rev. B* **79**, 241104 (2009).
- [66] A. E. Siegman, *Lasers* (University Science Books, Mill Valley, Calif, USA, 1986).

- [67] P. G. Ciarlet, *The Finite Element Method for Elliptic Problems* (North-Holland, Amsterdam, New York, Oxford, 1978).
- [68] G. Strang and G. J. Fix, *An Analysis of the Finite Element Method* (Prentice-Hall, Englewood Cliffs, New Jersey, 1973).
- [69] O. C. Zienkiewicz, *The Finite Element Method* (McGraw-Hill, London, 1977).
- [70] E. J. Smith, Z. Liu, Y. Mei, and O. G. Schmidt, *Nano Lett.* **10**, 1–5 (2009).
- [71] J. T. Katsikadelis, *Boundary Elements Theory and Applications* (Elsevier Science, Oxford, 2002).
- [72] T. Zhan, C. Xu, F. Zhao, Z. Xiong, X. Hu, G. Huang, Y. Mei, and J. Zi, *Appl. Phys. Lett.* **99**, 211104 (2011).
- [73] H. C. van de Hulst, *Light Scattering by Small Particles* (Dover, New York, 1981).
- [74] X. Hu, C. T. Chan, K.-M. Ho, and J. Zi, *Phys. Rev. Lett.* **106**, 174501 (2011).
- [75] Z. Ruan and S. Fan, *Phys. Rev. Lett.* **105**, 013901 (2010).
- [76] C. Strelow, C. M. Schultz, H. Rehberg, M. Sauer, H. Welsch, A. Stemmann, C. Heyn, D. Heitmann, and T. Kipp, *Phys. Rev. B* **85**, 155329 (2012).
- [77] K. M. Lee, P. T. Leung, and K. M. Pang, *J. Opt. Soc. Am. B* **16**, 1418–1430 (1999).
- [78] S. G. Johnson, M. Ibanescu, M. A. Skorobogatiy, O. Weisberg, J. D. Joannopoulos, and Y. Fink, *Phys. Rev. E* **65**, 066611 (2002).
- [79] L. Ma, S. Kiravittaya, V. A. B. Quinones, S. Li, Y. Mei, and O. G. Schmidt, *Opt. Lett.* **36**, 3840–3842 (2011).
- [80] F. Goos and H. Hänchen, *Ann. Phys.* **436**, 333–346 (1947).
- [81] E. Hecht, *Optics* (Addison-Wesley, Reading, Mass, 1998).
- [82] H. J. Moon, G. W. Park, S. B. Lee, K. An, and J. H. Lee, *Appl. Phys. Lett.* **84**, 4547–4549 (2004).
- [83] E. P. Ippen and C. V. Shank, *Appl. Phys. Lett.* **21**, 301–302 (1972).
- [84] T. Kobayashi and N. Byrne, *Appl. Phys. Lett.* **99**, 153307 (2011).
- [85] K. Dietrich, C. Strelow, C. Schliehe, C. Heyn, A. Stemmann, S. Schwaiger, S. Mendach, A. Mews, H. Weller, D. Heitmann, and T. Kipp, *Nano Lett.* **10**, 627–631 (2010).
- [86] A. Shevchenko, K. Lindfors, S. C. Buchter, and M. Kaivola, *Opt. Commun.* **245**, 349–353 (2005).
- [87] H. J. Moon, Y. T. Chough, and K. An, *Phys. Rev. Lett.* **85**, 3161–3164 (2000).
- [88] C. W. Chen, H. P. Chiang, D. P. Tsai, and P. T. Leung, *Appl. Phys. B* **107**, 111–118 (2012).
- [89] W. W. Deng, S. P. Wu, and G. X. Li, *Opt. Commun.* **285**, 2668–2674 (2012).
- [90] X. Chen, X. J. Lu, P. L. Zhao, and Q. B. Zhu, *Opt. Lett.* **37**, 1526–1528 (2012).
- [91] H. Gilles, S. Girard, and J. Hamel, *Opt. Lett.* **27**, 1421–1423 (2002).
- [92] M. Saito and K. Koyama, *J. Opt.* **14**, 065002 (2012).
- [93] K. Artmann, *Ann. Phys.-Berlin* **2**, 87–102 (1948).
- [94] S. Lacey, I. M. White, Y. Sun, S. I. Shopova, J. M. Cupps, P. Zhang, and X. D. Fan, *Opt. Exp.* **15**, 15523–15530 (2007).
- [95] G. C. Righini, Y. Dumeige, P. Feron, M. Ferrari, G. Nunzi Conti, D. Ristic, and S. Soria, *Riv. Nuovo Cimento* **34**, 435–488 (2011).
- [96] J. R. Schwesyg, T. Beckmann, A. S. Zimmermann, K. Buse, and D. Hacrtle, *Opt. Exp.* **17**, 2573–2578 (2009).
- [97] M. L. Gorodetsky, A. D. Pryamikov, and V. S. Ilchenko, *J. Opt. Soc. Am. B* **17**, 1051–1057 (2000).
- [98] P. K. Tien, *Appl. Opt.* **10**, 2395–2413 (1971).
- [99] V. B. Braginsky, M. L. Gorodetsky, and V. S. Ilchenko, *Phys. Lett. A* **137**, 393–397 (1989).
- [100] D. W. Vernooy, V. S. Ilchenko, H. Mabuchi, E. W. Streed, and H. J. Kimble, *Opt. Lett.* **23**, 247–249 (1998).
- [101] M. L. Gorodetsky, A. A. Savchenkov, and V. S. Ilchenko, *Opt. Lett.* **21**, 453–455 (1996).
- [102] J. Wang, T. Zhan, G. Huang, X. Cui, X. Hu, and Y. Mei, *Opt. Exp.* **20**, 18555–18567 (2012).
- [103] H.-J. Moon, G.-W. Park, S.-B. Lee, K. An, and J.-H. Lee, *Opt. Commun.* **235**, 401–407 (2004).
- [104] F. Zhao, T. Zhan, G. Huang, Y. Mei, and X. Hu, *Lab Chip* **12**, 3798–3802 (2012).
- [105] V. A. Bolans Quines, G. Huang, J. D. Plumhof, S. Kiravittaya, A. Rastelli, Y. Mei, and O. G. Schmidt, *Opt. Lett.* **34**, 2345–2347 (2009).
- [106] S. L. McCall, A. F. J. Levi, R. E. Slusher, S. J. Pearton, and R. A. Logan, *Appl. Phys. Lett.* **60**, 289–291 (1992).
- [107] B. E. Little and S. T. Chu, *Opt. Lett.* **21**, 1390–1392 (1996).
- [108] M. L. Gorodetsky and V. S. Ilchenko, *J. Opt. Soc. Am. B* **16**, 147–154 (1999).
- [109] F. Li, Z. T. Mi, and S. Vicknesh, *Opt. Lett.* **34**, 2915–2917 (2009).
- [110] F. Luan, E. Magi, T. X. Gong, I. Kabakova, and B. J. Eggleton, *Opt. Lett.* **36**, 4761–4763 (2011).
- [111] Y. Z. Sun and X. D. Fan, *Anal. Bioanal. Chem.* **399**, 205–211 (2011).
- [112] I. M. White, H. Oveys, X. Fan, T. L. Smith, and J. Y. Zhang, *Appl. Phys. Lett.* **89**, 191106 (2006).
- [113] J. D. Suter, I. M. White, H. Y. Zhu, H. D. Shi, C. W. Caldwell, and X. D. Fan, *Biosens. Bioelectron.* **23**, 1003–1009 (2008).
- [114] R. Ulrich and H. P. Weber, *App. Phys. Lett.* **20**, 38–40 (1972).
- [115] R. Ulrich and H. P. Weber, *Appl. Opt.* **11**, 428–434 (1972).
- [116] S. X. Dou, E. Toussaere, T. Ben-Messaoud, A. Potter, D. Josse, G. Kranzelbinder, and J. Zyss, *Appl. Phys. Lett.* **80**, 165–167 (2002).
- [117] S. V. Frolov, Z. V. Vardeny, and K. Yoshino, *Appl. Phys. Lett.* **72**, 1802–1804 (1998).
- [118] S. V. Frolov, M. Shkunov, Z. V. Vardeny, and K. Yoshino, *Phys. Rev. B* **56**, R4363–R4366 (1997).
- [119] S. I. Shopova, J. M. Cupps, P. Zhang, E. P. Henderson, S. Lacey, and X. D. Fan, *Opt. Exp.* **15**, 12735–12742 (2007).
- [120] C. H. Vannoy, A. J. Tavares, M. O. Noor, U. Udayasankar, and U. J. Krull, *Sensors* **11**, 9732–9763 (2011).
- [121] C. P. K. Manchee, V. Zamora, J. W. Silverstone, J. G. C. Veinot, and A. Meldrum, *Opt. Exp.* **19**, 21540–21551 (2011).
- [122] M. Kazes, D. Y. Lewis, Y. Ebenstein, T. Mokari, and U. Banin, *Adv. Mater.* **14**, 317–321 (2002).
- [123] X. L. Li, *J. Phys. D: Appl. Phys.* **41**, 193001 (2008).
- [124] E. Hecht, *Optics* (Addison-Wesley, Reding, Mass, 1998).
- [125] X. Yi, Y.-F. Xiao, Y. Li, Y.-C. Liu, B.-B. Li, Z.-P. Liu, and Q. Gong, *Appl. Phys. Lett.* **97**, 203705 (2010).

- [126] V. Zamora, A. Diez, M. V. Andres, and B. Gimeno, *Opt. Exp.* **15**, 12011–12016 (2007).
- [127] S. M. Harazim, W. Xi, C. K. Schmidt, S. Sanchez, and O. G. Schmidt, *J. Mater. Chem.* **22**, 2878–2884 (2012).
- [128] E. J. Smith, S. Schulze, S. Kiravittaya, Y. Mei, S. Sanchez, and O. G. Schmidt, *Nano Lett.* **11**, 4037–4042 (2011).
- [129] E. J. Smith, W. Xi, D. Makarov, I. Monch, S. Harazim, V. A. B. Quinones, C. K. Schmidt, Y. F. Mei, S. Sanchez, and O. G. Schmidt, *Lab Chip* **12**, 1917–1931 (2012).
- [130] V. A. B. Quinones, G. Huang, J. D. Plumhof, S. Kiravittaya, A. Rastelli, Y. Mei, and O. G. Schmidt, *Opt. Lett.* **34**, 2345–2347 (2009).
- [131] X. Yi, Y.-F. Xiao, Y.-C. Liu, B.-B. Li, Y.-L. Chen, Y. Li, and Q. Gong, *Phys. Rev. A* **83**, 023803 (2011).
- [132] a) M. Sumetsky, *Opt. Lett.* **35**, 2385–2387 (2010); b) N. Gaber, M. Malak, X. Yuan, K. N. Nquyen, P. Basset, E. Richalot, D. Angelescu, T. Bourouina, *Lab Chip*, **13**, 826–833, 2013
- [133] I. M. White, H. Oveys, and X. D. Fan, *Opt. Lett.* **31**, 1319–1321 (2006).
- [134] J. M. Ward, D. G. O’Shea, B. J. Shortt, M. J. Morrissey, K. Deasy, and S. G. N. Chormaic, *Rev. Sci. Instrum.* **77**, 083105 (2006).
- [135] M. Ding, G. S. Murugan, G. Brambilla, and M. N. Zervas, *Appl. Phys. Lett.* **100**, 081108 (2012).
- [136] A. F. Abouraddy, M. Bayindir, G. Benoit, S. D. Hart, K. Kuriki, N. Orf, O. Shapira, F. Sorin, B. Temelkuran, and Y. Fink, *Nature Mater.* **6**, 336–347 (2007).
- [137] G. Huang and Y. Mei, *Adv. Mater.* **24**, 2517–2546 (2012).
- [138] A. Cho, *Science* **313**, 164–165 (2006).
- [139] M. Yu, Y. Huang, J. Ballweg, H. Shin, M. Huang, D. E. Savage, M. G. Lagally, E. W. Dent, R. H. Blick, and J. C. Williams, *ACS Nano* **5**, 2447–2457 (2011).
- [140] V. Luchnikov, L. Ionov, and M. Stamm, *Macromol. Rapid Commun.* **32**, 1943–1952 (2011).
- [141] T. Angelova, N. Shtinkov, T. Ivanov, V. Donchev, A. Cantarero, C. Deneke, O. G. Schmidt, and A. Cros, *Appl. Phys. Lett.* **100**, 201904 (2012).
- [142] M. Maqbool, K. Main, and M. Kordesch, *Opt. Lett.* **35**, 3637–3639 (2010).
- [143] D. O’Carroll, I. Lieberwirth, and G. Redmond, *Nature Nanotechnol.* **2**, 180–184 (2007).
- [144] Z. Hou, G. Li, H. Lian, and J. Lin, *J. Mater. Chem.* **22**, 5254–5276 (2012).
- [145] J. D. Lin, Y. Z. Huang, Q. F. Yao, X. M. Lv, Y. D. Yang, J. L. Xiao, and Y. Du, *Electron. Lett.* **47**, 929–930 (2011).
- [146] K. Scholten, X. Fan, and E. T. Zellers, *Appl. Phys. Lett.* **99**, 141108 (2011).
- [147] S. Vicknesh, F. Li, and Z. Mi, *Appl. Phys. Lett.* **94**, 081101 (2009).
- [148] D. Psaltis, S. R. Quake, and C. Yang, *Nature* **442**, 381–386 (2006).
- [149] S. C. Terry, J. H. Jerman, and J. B. Angell, *IEEE Trans. Electron Devices* **26**, 1880–1886 (1979).
- [150] H. J. Moon, Y. T. Chough, J. B. Kim, K. W. An, J. H. Yi, and J. Lee, *Appl. Phys. Lett.* **76**, 3679–3681 (2000).
- [151] D. J. Thurmer, C. Deneke, Y. Mei, and O. G. Schmidt, *Appl. Phys. Lett.* **89**, 223507 (2006).
- [152] N. Tessler, *Adv. Mater.* **11**, 363–370 (1999).
- [153] I. D. W. Samuel, E. B. Namdas, and G. A. Turnbull, *Nature Photon.* **3**, 546–549 (2009).
- [154] H. Altug, D. Englund, and J. Vuckovic, *Nature Phys.* **2**, 484–488 (2006).
- [155] I. D. W. Samuel and G. A. Turnbull, *Chem. Rev.* **107**, 1272–1295 (2007).
- [156] L. N. Deryugin, I. V. Cheremiskin, and T. K. Chekhlova, *Sov. J. Quant. Electron.* **5**, 439–442 (1975).
- [157] S. V. Frolov, A. Fujii, D. Chinn, M. Hirohata, R. Hidayat, M. Taraguchi, T. Masuda, K. Yoshino, and Z. V. Vardeny, *Adv. Mater.* **10**, 869–872 (1998).
- [158] A. V. Malko, A. A. Mikhailovsky, M. A. Petruska, J. A. Hollingsworth, H. Htoon, M. G. Bawendi, and V. I. Klimov, *Appl. Phys. Lett.* **81**, 1303–1305 (2002).
- [159] M. Kazes, D. Y. Lewis, and U. Banin, *Adv. Funct. Mater.* **14**, 957–962 (2004).
- [160] Y. Sun, S. I. Shopova, C.-S. Wu, S. Arnold, and X. Fan, *Proc. Natl. Acad. Sci. USA* **107**, 16039–16042 (2010).
- [161] S. I. Shopova, J. M. Cupps, P. Zhang, E. P. Henderson, S. Lacey, and X. Fan, *Opt. Exp.* **15**, 12735–12742 (2007).
- [162] K. E. Sapsford, L. Berti, and I. L. Medintz, *Angew. Chem. Int. Ed.* **45**, 4562–4588 (2006).
- [163] O. Shapira, K. Kuriki, N. D. Orf, A. F. Abouraddy, G. Benoit, J. F. Viens, A. Rodriguez, M. Ibanescu, J. D. Joannopoulos, Y. Fink, and M. M. Brewster, *Opt. Exp.* **14**, 3929–3935 (2006).
- [164] A. M. Stolyarov, L. Wei, O. Shapira, F. Sorin, S. L. Chua, J. D. Joannopoulos, and Y. Fink, *Nature Photon.* **6**, 229–233 (2012).
- [165] A. A. Fotiadi and P. Megret, *Nature Photon.* **6**, 217–219 (2012).
- [166] Y. Sun, J. D. Suter, and X. D. Fan, *Opt. Lett.* **34**, 1042–1044 (2009).
- [167] G. Farca, S. I. Shopova, and A. T. Rosenberger, *Opt. Exp.* **15**, 17443–17448 (2007).
- [168] H. Li and X. D. Fan, *Appl. Phys. Lett.* **97**, 011105 (2010).
- [169] J. T. Gohring, P. S. Dale, and X. D. Fan, *Sens. Actuators B-Chem.* **146**, 226–230 (2010).
- [170] X. D. Fan, I. M. White, S. I. Shopova, H. Y. Zhu, J. D. Suter, and Y. Z. Sun, *Anal. Chim. Acta* **620**, 8–26 (2008).
- [171] H. Li, Y. B. Guo, Y. Z. Sun, K. Reddy, and X. D. Fan, *Opt. Exp.* **18**, 25081–25088 (2010).
- [172] H. Y. Zhu, I. M. White, J. D. Suter, M. Zourob, and X. D. Fan, *Anal. Chem.* **79**, 930–937 (2007).
- [173] H. Y. Zhu, I. M. White, J. D. Suter, M. Zourob, and X. D. Fan, *Analyst* **133**, 356–360 (2008).
- [174] H. Y. Zhu, P. S. Dale, C. W. Caldwell, and X. D. Fan, *Anal. Chem.* **81**, 9858–9865 (2009).
- [175] C. P. K. Manchee, V. Zamora, J. W. Silverstone, J. G. C. Veinot, and A. Meldrum, *Opt. Exp.* **19**, 21540 (2011).
- [176] C. Deneke and O. G. Schmidt, *Appl. Phys. Lett.* **85**, 2914–2916 (2004).
- [177] M. T. Todaro, L. Blasi, C. Giordano, A. Rizzo, R. Cingolani, G. Gigli, A. Passaseo, and M. D. Vittorio, *Nanotechnology* **21**, 245305 (2010).
- [178] E. J. Smith, S. Schulze, S. Kiravittaya, Y. F. Mei, S. Sanchez, and O. G. Schmidt, *Nano Lett.* **11**, 4037–4042 (2010).
- [179] B. Yuan, Y. Jin, Y. Sun, D. Wang, J. Sun, Z. Wang, W. Zhang, and X. Jiang, *Adv. Mater.* **24**, 890–896 (2012).

- [180] V. S. Ilchenko, M. L. Gorodetsky, and S. P. Vyatchanin, *Opt. Commun.* **107**, 41–48 (1994).
- [181] A. L. Huston and J. D. Eversole, *Opt. Lett.* **18**, 1104–1106 (1993).
- [182] A. Tulek and Z. V. Vardeny, *Appl. Phys. Lett.* **91**, 121102 (2007).
- [183] P. Mach, M. Dolinski, K. W. Baidwin, and J. A. Rogers, *Appl. Phys. Lett.* **80**, 4294 (2002).
- [184] D. Erickson, D. Sinton, and D. Psaltis, *Nature Photon.* **5**, 583–590 (2011).
- [185] Z. Liu, H. Lee, Y. Xiong, C. Sun, and X. Zhang, *Science* **315**, 1686–1686 (2007).
- [186] C. Deneke, U. Zschieschang, H. Klauk, and O. G. Schmidt, *Appl. Phys. Lett.* **89**, 263110 (2006).
- [187] C. Deneke, W. Sigle, U. Eigenthaler, P. A. van Aken, G. Schutz, and O. G. Schmidt, *Appl. Phys. Lett.* **90**, 263107 (2007).
- [188] C. Deneke, R. Songmuang, N. Y. Jin-Phillipp, and O. G. Schmidt, *J. Phys. D: Appl. Phys.* **42**, 103001 (2009).
- [189] P. Yang and J.-M. Tarascon, *Nature Mater.* **11**, 560–563 (2012).
- [190] W. Li, G. Huang, H. Yan, J. Wang, Y. Yu, X. Hu, X. Wu, and Y. Mei, *Soft Matter* **8**, 3103–3107 (2012).
- [191] Y. Yao, J. Yao, V. K. Narasimhan, Z. Ruan, C. Xie, S. Fan, and Y. Cui, *Nature Commun.* **3**, 664 (2011).
- [192] G. Anetsberger, R. Riviere, A. Schliesser, O. Arcizet, and T. J. Kippenberg, *Nature Photon.* **2**, 627–633 (2008).
- [193] X. Sun, K. Y. Fong, C. Xiong, W. H. P. Pernice, and H. X. Tang, *Opt. Exp.* **19**, 22316–22321 (2011).
- [194] K. Srinivasan, H. Miao, M. T. Rakher, M. Davanco, and V. Aksyuk, *Nano Lett.* **11**, 791–797 (2011).

TAKE A LOOK AT WILEY'S RANGE OF OPTICAL METROLOGY BOOKS

Authored and edited by experts in the field, each utilising the current research findings in the most prominent topics.



For a full listing of titles available and to order, please visit www.wiley.com/go/physics

WILEY

14-64355